# The MJO on the Equatorial Beta Plane: An Eastward-Propagating Rossby Wave Induced by Meridional Moisture Advection

FIAZ AHMED[a]

[a] *Department of Atmospheric and Oceanic Sciences, University of California, Los Angeles, Los Angeles, California*

(Manuscript received 11 March 2021, in final form 1 July 2021)

ABSTRACT: Linearized wave solutions on the equatorial beta plane are examined in the presence of a background meridional moisture gradient. Of interest is a slow, eastward-propagating $n = 1$ mode that is unstable at planetary scales and only exists for a small range of zonal wavenumbers ($\lesssim$6). The mode dispersion curve appears as an eastward extension of the westward-propagating equatorial Rossby wave solution. This mode is therefore termed the eastward-propagating equatorial Rossby wave (ERW). The zonal wavenumber-2 ERW horizontal structure consists of a low-level equatorial convergence center flanked by quadrupole off-equatorial gyres, and resembles the horizontal structure of the observed MJO. An analytic, leading-order dispersion relationship for the ERW shows that meridional moisture advection imparts eastward propagation, and that the smallness of a gross moist stability–like parameter contributes to the slow phase speed. The ERW is unstable near planetary scales when low-level easterlies moisten the column. This moistening could come from either zonal moisture advection or surface fluxes or a combination thereof. When westerlies instead moisten the column, the ERW is damped and the westward-propagating long Rossby wave is unstable. The ERW does not exist when the meridional moisture gradient is too weak. A moist static energy budget analysis shows that the ERW scale selection is partly due to finite-time-scale convective adjustment and less effective zonal wind–induced moistening at smaller scales. Similarities in the phase speed, preferred scale, and horizontal structure suggest that the ERW is a beta-plane analog of the MJO.

KEYWORDS: Madden-Julian oscillation; Advection; Moisture/moisture budget; Primitive equations model

## 1. Introduction

Our understanding of tropical waves owes much to the study of perturbations on the equatorial beta plane (Matsuno 1966). A remarkable correspondence exists between linearized beta-plane solutions and observed tropical waves (Takayabu 1994; Wheeler and Kiladis 1999; Kiladis et al. 2009)—in both the wave dispersion properties and horizontal structures. Equatorial Rossby waves, inertio-gravity waves, the mixed Rossby–gravity wave and the Kelvin wave all have analogous beta-plane solutions (Kiladis et al. 2009).

A beta-plane analog for the Madden Julian Oscillation (MJO; Madden and Julian 1971, 1994; Zhang 2005) is noticeably absent in the simplest, dry version of the model. The salient properties of the observed MJO are that it propagates eastward at slow speeds ($\sim$5 m s$^{-1}$) and exists at near-planetary scales (Madden and Julian 1971, 1994). A secondary attribute is the peculiar horizontal structure. At low levels, an equatorial convergence center is flanked by two pairs of off-equatorial gyres: a pair of cyclonic gyres to the west and a pair of anticyclonic gyres to the east (Rui and Wang 1990; Hendon and Salby 1994; Hendon and Liebmann 1994; Kiladis et al. 2005). One advantage of identifying beta-plane analogs for the MJO is that the phase speed, preferred horizontal scale and the horizontal structure are available simultaneously as solutions of an eigenvalue problem.

While several reasonable theoretical explanations for the MJO are available (see review in Zhang et al. 2020), only a subset of these look to relate the MJO to beta-plane solutions. Slow, eastward-propagating modes with planetary scale selection do exist in beta-plane models with prognostic moisture variations (Neelin and Yu 1994; Fuchs and Raymond 2002, 2017). However, these modes were derived out of a system with zero meridional wind. Their horizontal structures are consequently not fully consistent with that of the observed MJO. Recently, Emanuel (2020) derived an eigenmode of the equatorial beta plane with both propagation speed and horizontal structure consistent with the observed MJO. This is a promising development since it shows that beta-plane MJO analogs do exist as a single eigenmode. This study takes a closer look at this MJO-like eigenmode on the beta plane. In contrast to studies listed above, the equatorial beta plane used here is equipped with a background meridional moisture gradient.

Two separate lines of evidence suggest that the background meridional moisture gradient plays an important role in equatorial wave dynamics. The first line of evidence follows from idealized models. Sobel et al. (2001) report that a background meridional humidity gradient on the $f$ plane allows a slow, eastward-propagating mode to emerge. Similar modes have also been noted in both linear and nonlinear models with background moisture gradients (Sukhatme 2014; Monteiro and Sukhatme 2016; Wang et al. 2016; Suhas and Sukhatme 2020; Wang and Chen 2017). Sukhatme (2014) derived numerical dispersion relationships for this mode, and also showed that it is destabilized by a positive zonal moisture gradient. Suhas and Sukhatme (2020) later identified this mode as a moist Rossby

Supplemental information related to this paper is available at the Journals Online website: https://doi.org/10.1175/JAS-D-21-0071.s1.

*Corresponding author*: Fiaz Ahmed, fiaz@ucla.edu

DOI: 10.1175/JAS-D-21-0071.1

wave. In contrast, Wang et al. (2016) and Wang and Chen (2017) characterize a similar solution in their model as a coupled Kelvin–Rossby mode (based on its horizontal structure), and identify it with the MJO. Despite the diverging interpretations of their results, these studies point to the importance of the meridional moisture gradient in inducing modes with possible relevance for the MJO. The second line of evidence follows from composite MJO studies using either reanalyses (Kim et al. 2014; Adames and Wallace 2015; Kim et al. 2017; DeMott et al. 2018; Kang et al. 2021) or climate models (Jiang 2017; Gonzalez and Jiang 2017; DeMott et al. 2019; Kang et al. 2020; Jiang et al. 2020). These studies demonstrate that moisture advection by MJO winds flowing across the background meridional moisture gradient aids MJO propagation. Jiang et al. (2020) also note that MJO-like variance significantly diminishes with reductions in the meridional moisture gradient.

It appears that the meridional moisture gradient is an important—but underemphasized—property of the background state on the equatorial beta plane. The main objective of this study is to check if this property affects the wave solutions on the beta plane. In section 2, a beta-plane model with a background meridional moisture gradient is introduced. In section 3, an eigenvalue problem is set up for the model. In section 4, it is shown that the beta-plane solutions are qualitatively altered in the presence of the meridional moisture gradient. A slow, eastward-propagating mode that is unstable at the planetary scale emerges as a valid solution to the eigenvalue problem. This mode is identified as an eastward-propagating equatorial Rossby wave. The eigenfunction associated with this mode is shown to resemble the observed MJO horizontal structure. In section 5, the leading-order dispersion relationship is derived for this mode; the mechanisms that govern the mode propagation and scale selection are also explored. Section 6 details the sensitivity of this mode to important model parameters. The relevance of the results for the MJO are discussed in section 7 and the study is summarized in section 8.

## 2. Model setup

### a. Governing equations

We begin with a system of inviscid, linearized equations on the equatorial beta plane, similar to the models of Neelin and Yu (1994) and Ahmed et al. (2021, hereafter A21):

$$\frac{\partial u}{\partial t} - \beta y v + \frac{\partial \phi}{\partial x} = 0, \tag{1}$$

$$\frac{\partial v}{\partial t} + \beta y u + \frac{\partial \phi}{\partial y} = 0, \tag{2}$$

$$\frac{\partial u}{\partial x} + \frac{\partial v}{\partial y} = -\frac{\partial \omega}{\partial p}, \tag{3}$$

$$\frac{\partial \phi}{\partial p} = -\frac{R_d}{p} T, \tag{4}$$

$$\frac{\partial \langle T \rangle}{\partial t} + \left\langle \omega \frac{\partial \overline{S}}{\partial p} \right\rangle = \langle Q_c \rangle + \langle Q_r \rangle, \tag{5}$$

$$\frac{\partial \langle q \rangle}{\partial t} + \left\langle u \frac{\partial \overline{q}}{\partial x} \right\rangle + \left\langle v \frac{\partial \overline{q}}{\partial y} \right\rangle + \left\langle \omega \frac{\partial \overline{q}}{\partial p} \right\rangle = E - \langle Q_c \rangle. \tag{6}$$

The linearized zonal, meridional, and vertical pressure velocities are $u$, $v$ and $\omega$, respectively. The linearized geopotential and temperature are $\phi$ and $T$, respectively. Here, (1) and (2) are the horizontal momentum equations. The continuity equation is (3), and the hydrostatic balance along with the ideal gas law yields (4). The meridional gradient of the Coriolis parameter is $\beta$ and the dry-air gas constant is $R_d$. The column integration operation is denoted by $\langle \cdots \rangle$. The budget equations for the linearized, column-integrated temperature $\langle T \rangle$ and moisture $\langle q \rangle$ are in (5) and (6), respectively; the column-integrated latent and radiative heating rates are $\langle Q_c \rangle$ and $\langle Q_r \rangle$, respectively. The background values of dry static energy and moisture are $\overline{S}$ and $\overline{q}$, respectively. The moisture budget in (6) has been multiplied by the latent heat of vaporization $L_v$, and divided by the heat capacity of dry air $c_p$ so that $\langle T \rangle$ and $\langle q \rangle$ have the same units of K kg m$^{-2}$. In (6), the column-integrated moisture loss due to precipitation is assumed equal to the column latent heating $\langle Q_c \rangle$. Anomalies in surface evaporation are denoted by $E$.

### b. Vertical truncation

Following an oft-used truncation procedure in tropical dynamics (Emanuel 1987; Neelin and Yu 1994; Neelin and Zeng 2000; Sobel et al. 2001; Bretherton and Sobel 2002; Adames and Kim 2016; Khairoutdinov and Emanuel 2018; Adames et al. 2019; A21), a single deep vertical structure—corresponding to moist adiabatic variations—is assumed to represent temperature perturbations. A rigid lid is also assumed at the top of the troposphere. These assumptions can be relaxed to include multiple vertical structures (Mapes 2000; Majda and Shefter 2001; Khouider and Majda 2006; Kuang 2008; Khouider and Majda 2008; Stechmann and Hottovy 2017), a radiating upper boundary (Yano and Emanuel 1991; Raymond and Fuchs 2007; Fuchs et al. 2012), and an independently varying boundary layer (Wang and Rui 1990; Wang et al. 2016; Wang and Chen 2017). The main results of this study are, however, available without these extensions.

As in Neelin and Zeng (2000), the vertical truncation for the temperature, baroclinic winds and the vertical velocity are given by

$$T(x,y,t,p) = T_1(x,y,t)A(p),$$

$$u(x,y,t,p) = u_1(x,y,t)V(p),$$

$$v(x,y,t,p) = v_1(x,y,t)V(p),$$

$$\omega(x,y,t,p) = \omega_1(x,y,t)\Omega(p).$$

Here $A(p)$, $V(p)$, and $\Omega(p)$ are the vertical structures for temperature, baroclinic horizontal wind and vertical velocity perturbations, respectively (shown in the appendix); $T_1$, $u_1$, $v_1$, and $\omega_1$ contain the horizontal and time dependence. Note that $V(p)$ is such that positive perturbations in $u_1$ and $v_1$ correspond to *negative* low-level and *positive* upper-level wind perturbations (Fig. A1 in appendix). Also note that $V(p)$ and $\Omega(p)$ are linked through the continuity equation, (3).

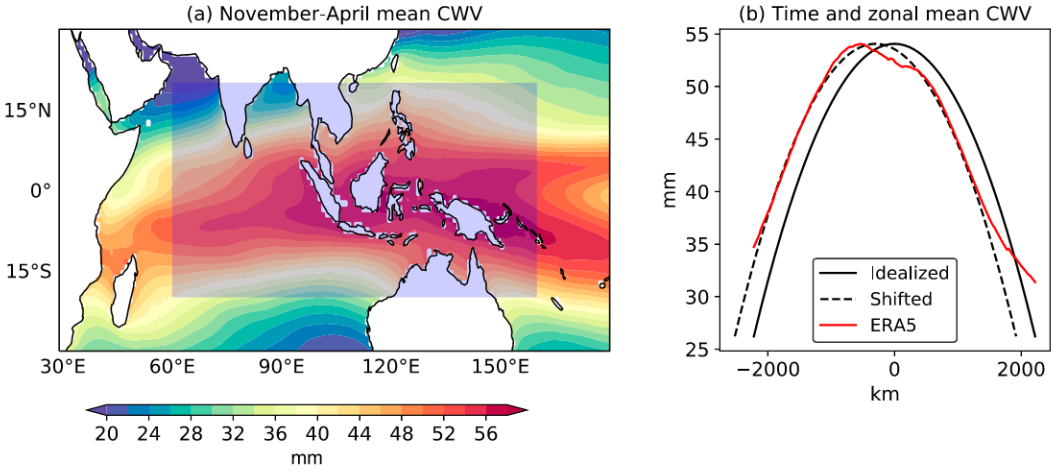


FIG. 1. (a) The CWV field from ERA5 averaged over months November–April for years 2002–14. The gray shading represents the domain chosen for the zonal averaging of CWV. (b) The red curve is the zonally averaged ERA5 CWV profile, the solid black curve is the background meridional moisture profile captured using (9), and the dashed black curve is the solid black curve shifted southward to overlie the ERA5 profile.

### c. *Parameterizations*

#### 1) MERIDIONAL MOISTURE ADVECTION

The background moisture field, $\overline{q}$ is assumed to have a vertical structure $b(p)$ (Fig. A1 in the appendix). It is also assumed that $\overline{q}$ varies quadratically in the meridional direction such that

$$\overline{q}(x,y,p) = \left[\overline{q}_o(x) - \frac{\sigma_{yo} y^2}{2}\right] b(p). \tag{7}$$

Here $\sigma_{yo}$ is a positive parameter that denotes the strength of the meridional moisture gradient. Any zonal variations in the background moisture field are contained within $\overline{q}_o(x)$. Using (7) it follows that

$$\left\langle v \frac{\partial \overline{q}}{\partial y} \right\rangle = -v_1 \langle Vb \rangle \sigma_{yo} y = v_1 \sigma_y y, \tag{8}$$

where $\sigma_y$ is a parameter that contains information about the meridional moisture gradient $\partial_y \overline{q}$, in addition to the vertical structures $V(p)$ and $b(p)$. If the background moisture field decreases away from the equator, then $\sigma_y > 0$. In this case, according to (8), low-level equatorward flows dry the column whereas low-level poleward flows moisten the column. To estimate $\sigma_y$, the expression in (7) is first vertically integrated to give

$$\langle \overline{q} \rangle (x,y) = \overline{q}_o(x) \langle b \rangle - \sigma_{y0} \langle b \rangle \frac{y^2}{2}. \tag{9}$$

The relationship in (9) is then fit to the ERA5 (Hersbach et al. 2020) column water vapor (CWV) field. This fit yields $\sigma_{y0}$, from which $\sigma_y$ is inferred using (8).

As stated in the introduction, a main motivation for the present study is the apparent importance of the meridional moisture gradient for MJO dynamics. The estimate of $\sigma_y$ is therefore focused on the region and season with the most observed MJO variability: the Indo-Pacific warm pool for the months November–April (Zhang and Dong 2004). The ERA5 CWV is zonally averaged over the shaded domain shown in Fig. 1a for the months November–April over the years 2002–14. This averaged CWV field is fit to (9) as shown in Fig. 1b. The value of $\overline{q}_o(x)\langle b \rangle$ is taken to be the maximum averaged CWV value along the meridional direction (~54 mm). A value of $\sigma_{yo}\langle b \rangle = 1.13 \times 10^{-11}\,\mathrm{kg\,m^{-4}}$ yields the solid black line in Fig. 1b. Multiplying this value by $L_v/c_p$ and using the relationship between $\sigma_{y0}$ and $\sigma_y$ from (8) yields the reference value of $\sigma_y = 9 \times 10^{-9}\,\mathrm{K\,kg\,m^{-4}}$. The vertical structures $V(p)$ and $b(p)$ are used in this estimation (see the appendix).

The dashed black line in Fig. 1b is the solid black line shifted southward to better display the goodness-of-fit with the ERA5 meridional CWV distribution. For simplicity, the slight asymmetry in the ERA5 CWV distribution around the equator is ignored in (7). This asymmetry can be included with an additional term in (7) that is linear in $y$. It has been verified that this inclusion does not qualitatively impact the primary results.

#### 2) MOISTENING EFFECTS OF ZONAL WIND

Following previous studies (Sobel and Maloney 2013; Adames and Kim 2016; Adames et al. 2019, A21), a single parameter is used to combine the effects of surface evaporation and zonal moisture advection:

$$\left\langle u \frac{\partial \overline{q}}{\partial x} \right\rangle - E = -u_1 \sigma_x, \tag{10}$$

where $\sigma_x$ subsumes the effects of wind-induced surface heat exchange (WISHE; Neelin et al. 1987; Emanuel 1987; Fuchs and Raymond 2017) and the background zonal moisture gradient (Adames et al. 2019). According to Sobel and Maloney (2013) and Adames and Kim (2016), $\sigma_x$ can also be endowed with the effects of synoptic-scale eddy moisture transports (Maloney and Dickinson 2003; Maloney 2009) and boundary layer frictional moisture convergence (Wang 1988; Hsu and Li 2012;

Adames and Wallace 2014). Ultimately, the governing equations are indifferent to how $\sigma_x$ is partitioned between its various subeffects. The only interpretation of consequence is that when $\sigma_x > 0$, low-level easterly perturbation winds ($u_1 > 0$) act as an effective column moisture source, while low-level westerly perturbations ($u_1 < 0$) act as an effective sink. Conversely, when $\sigma_x < 0$, low-level perturbation westerlies are a column moisture source, while easterlies are a column moisture sink. One caveat on the interpretation of $\sigma_x$ is that as the horizontal scale approaches wavenumber 0, it may not be meaningful to identify $\sigma_x$ with a zonal moisture gradient. Given the inclusive nature of $\sigma_x$, its value is subject to some uncertainty (Sobel and Maloney 2013). As will be shown later, the sign of this parameter is more consequential to our results than its exact value. The reference value of $\sigma_x$ is therefore arbitrarily chosen to be $5 \times 10^{-4}$ K kg m$^{-3}$. The impacts of varying this parameter on the solutions are shown in section 6a.

#### 3) DIABATIC HEATING

Following Ahmed et al. (2020) and A21, precipitation—assumed equivalent to column-integrated latent heating—is parameterized with an adjustment-based scheme involving moisture and temperature perturbations:

$$\langle Q_c \rangle = \varepsilon_q \langle q \rangle - \varepsilon_t \langle T \rangle . \tag{11}$$

Here $\varepsilon_q$ and $\varepsilon_t$ represent the sensitivity of convection to perturbations in column-integrated moisture and temperature, respectively. Expression (11) is the linearized version of the nonlinear precipitation closure developed in Ahmed et al. (2020), and is empirically informed by the tropical precipitation–buoyancy relationship (Ahmed and Neelin 2018; Schiro et al. 2018; Adames et al. 2021). This closure implicitly accounts for influences on convection due to variations in both free tropospheric moisture (Brown and Zhang 1997; Bretherton et al. 2004; Holloway and Neelin 2009; Kuo et al. 2017) and lower-tropospheric temperature (Mapes 2000; Raymond et al. 2003; Raymond and Fuchs 2007; Kuang 2008). The reference values for $\varepsilon_q$ and $\varepsilon_t$ follow from A21.

Variations in column-integrated radiative heating $\langle Q_r \rangle$ are assumed to occur in proportion to $\langle Q_c \rangle$ (Fuchs and Raymond 2002; Su and Neelin 2002; Lin and Mapes 2004):

$$\langle Q_r \rangle = r \langle Q_c \rangle , \tag{12}$$

where $r$ is the cloud–radiative feedback parameter (Kim et al. 2015). Estimates from previous studies (Fuchs and Raymond 2002; Bretherton and Sobel 2002; Peters and Bretherton 2005) inform the reference value for $r$ (=0.2).

### d. Meridional separation and complex exponentials

The meridional dependence in the state variables is separated from the zonal and temporal dependence; zonal and temporal variations are then assumed to be given by complex exponentials. For example,

$$v_1(x, y, t) = \tilde{v}_1(y) \exp(\lambda t + ikx), \tag{13}$$

where $\tilde{v}_1(y)$ contains the meridional dependence (and the amplitude); $\lambda$ is the frequency and $k$ is the wavenumber. This procedure is repeated for $u_1$, $\omega_1$, $T_1$, and $\langle q \rangle$, following which Eqs. (1)–(6) reduce to

$$\lambda u_1 - \beta y v_1 + \frac{ikc^2}{M_s} \langle T \rangle = 0 , \tag{14}$$

$$\lambda v_1 + \beta y u_1 + \frac{c^2}{M_s} \partial_y \langle T \rangle = 0 , \tag{15}$$

$$iku_1 + \partial_y v_1 = -\omega_1 , \tag{16}$$

$$[\lambda + \varepsilon_t (1 + r)] \langle T \rangle - \omega_1 M_s - \varepsilon_q (1 + r) \langle q \rangle = 0 , \tag{17}$$

$$(\lambda + \varepsilon_q) \langle q \rangle - \sigma_x u_1 + \sigma_y y v_1 + \omega_1 M_q - \varepsilon_t \langle T \rangle = 0. \tag{18}$$

In deriving the equations above, (4) is used to relate $\phi$ to $\langle T \rangle$. The first baroclinic dry gravity wave speed is $c$, which enters the equation set through the relationship: $c^2 = R_d M_s / \langle A \rangle$ (Sugiyama 2009; Adames and Kim 2016). The value of $c$ is taken to be 50 m s$^{-1}$. The parameterizations for meridional moisture advection in (8), the moistening effects of zonal wind in (10) and diabatic heating in (11)–(12) have also been used in deriving (14)–(18).

The positive parameters $M_s$ and $M_q$ are the gross dry stability and gross moisture stratification, respectively (Yu et al. 1998). They contain information about the vertical profiles of the background dry static energy $\overline{S}$ and moisture $\overline{q}$. Strictly speaking, the expression in (7) implies that $M_q$ ought to have both zonal and meridional variations. However, for the sake of tractability, this spatial dependence in $M_q$ is neglected. The relative gross moist stability, $m$ (Neelin and Held 1987; Raymond et al. 2009) is now defined using $M_s$ and $M_q$:

$$m = \frac{M_s - M_q}{M_s} . \tag{19}$$

To keep the ensuing expressions compact, four new parameters are now introduced:

$$\varepsilon_a = \varepsilon_q + \varepsilon_t (1 + r) , \tag{20}$$

$$m_{\text{eff}} = m(1 + r) - r , \tag{21}$$

$$\xi_x = \frac{\sigma_x}{M_s} , \tag{22}$$

$$\xi_y = \frac{\sigma_y}{M_s} . \tag{23}$$

The effective convective adjustment time scale (Ahmed et al. 2020, A21) is $\varepsilon_a$. The influence of cloud–radiative feedbacks on the gross moist stability enters through the effective gross moist stability $m_{\text{eff}}$ (Su and Neelin 2002; Neelin and Su 2005; Sobel and Maloney 2012; Adames and Kim 2016). Since $m_{\text{eff}}$ is a property of the time-independent background state, its reference value is taken to be positive (=0.1) following arguments from Inoue and Back (2017) and Fuchs and Raymond (2017). The impacts of perturbing $m_{\text{eff}}$ away from this value are detailed in section 6a. Both $\xi_x$ and $\xi_y$ are parameters of convenience; these parameters are dimensional and have differing units from one another.

## 3. The eigenvalue problem

Equations (14)–(18) are combined by (i) eliminating $\langle q \rangle$ between (17) and (18), (ii) eliminating $\omega_1$ using (16), and (iii) eliminating $\langle T \rangle$ and $u_1$ using (14) and (15). The result is a second-order ODE that yields an eigenvalue problem in $\tilde{v}_1$:

$$\frac{d^2\tilde{v}_1}{dy^2} - C_0 y \frac{d\tilde{v}_1}{dy} = -(C_1 - C_2 y^2)\tilde{v}_1, \tag{24}$$

where

$$C_0 = \frac{\varepsilon_q(1+r)}{\lambda + m_{\text{eff}}\varepsilon_q}\left(\frac{\xi_x \beta}{\lambda} - \xi_y\right), \tag{25}$$

$$C_1 = \frac{ik\beta}{\lambda} - k^2 - \frac{\lambda^2(\lambda+\varepsilon_a)}{c^2(\lambda + m_{\text{eff}}\varepsilon_q)} - \frac{ik\xi_x\varepsilon_q(1+r)}{(\lambda + m_{\text{eff}}\varepsilon_q)} - C_0, \tag{26}$$

$$C_2 = \frac{\beta^2}{c^2}\left(\frac{\lambda+\varepsilon_a}{\lambda + m_{\text{eff}}\varepsilon_q}\right) + \frac{ik\beta\xi_y\varepsilon_q(1+r)}{\lambda(\lambda + m_{\text{eff}}\varepsilon_q)}. \tag{27}$$

The ODE in (24) is similar in form to those derived for beta-plane systems with nonzero meridional wind (Matsuno 1966; Emanuel 1993; Fuchs and Raymond 2005; Fuchs-Stone et al. 2019; Emanuel 2020). The one noteworthy difference from previous studies is the additional influence of meridional moisture advection, which enters through $\xi_y$. Simply removing convection from the system by setting $\varepsilon_a = \varepsilon_q = 0$ in (24)–(27) is sufficient to recover the ODE for the dry beta plane (Matsuno 1966).

Solving (24) yields the dispersion relationship:

$$C_1 + \frac{C_0}{2} = \pm(2n+1)\sqrt{C_2 + \frac{C_0^2}{4}}, \tag{28}$$

where $n$ is a nonnegative integer that denotes the meridional mode. The eigenfunctions that describe the horizontal structure of the linearized solutions are complex-valued parabolic cylinder functions:

$$\tilde{v}_1(y) = \exp\left[\frac{-y^2}{2}\left(\pm\sqrt{C_2 + \frac{C_0^2}{4}} - \frac{C_0}{2}\right)\right] H_n\left[y\left(C_2 + \frac{C_0^2}{4}\right)^{1/4}\right], \tag{29}$$

where $H_n[\cdots]$ is the $n$th-order Hermite polynomial. Only the real part of (29) is physically meaningful. Both the integer $n$ and the sign preceding the square root in (29) must match their counterparts in (28). A nondimensional meridional inverse-scale parameter $S_y$ is now defined as

$$S_y = \text{Re}\left[\pm\sqrt{C_2 + \frac{C_0^2}{4}} - \frac{C_0}{2}\right]\frac{c}{\beta}, \tag{30}$$

where $\text{Re}[\cdots]$ denotes the real part. A condition for physically meaningful solutions to the eigenvalue problem (24) is that the meridional inverse-scale parameter be positive:

$$S_y > 0. \tag{31}$$

This is the same as requiring that the eigenfunctions in (29) vanish as $|y| \to \infty$. When (31) is satisfied, the meridional scale of the eigenfunctions in (29) is proportional to $1/\sqrt{S_y}$.

## 4. Counterpropagating Rossby waves

### a. Growth rate and phase speed

When written out fully, the dispersion relationship in (28) yields an eighth-order polynomial in $\lambda$ (see the appendix). For fixed $n$, there are eight possible solutions, out of which only those that satisfy (31) are permissible. Across a large portion of the parameter space, three valid solutions always exist with clear analogs in the dry case: the westward-propagating equatorial Rossby wave (WRW), and the eastward and westward-propagating inertio-gravity waves (EIGs and WIGs). However, certain parameter regimes permit additional solutions with possible geo-physical relevance and without analogs in the dry case.

The dispersion relationship (28) is solved using a numerical root solver (*NSolve* in Mathematica) using the reference parameter set detailed in Table 1. The permissible solutions for the $n = 1$ case are shown in Fig. 2. Solutions from the dry case (the Matsuno solutions) are also shown for comparison. Moist analogs for the inertio-gravity wave and WRW modes are seen in Fig. 2a—although with quantitative differences from the Matsuno solutions. There also exists an additional eastward-propagating solution for a small range of spatial scales (zonal wavenumber $\lesssim 6$) with no counterpart in the dry case. This solution appears as a continuous extension of the WRW solution across wavenumber 0—seen clearly in Figs. 2c and 2d. This property prompts the label *eastward-propagating equatorial Rossby wave* (ERW) to describe this solution. Analytic approximations for the dispersion relationships also reveal algebraic connections between the ERW and WRW, which are discussed in section 5.

The dry solutions are neutral (Figs. 2b,d). The moist solutions can be neutral, growing or decaying. The ERW is unstable for a small range of wavenumbers near the planetary scale (zonal wavenumbers $\lesssim 3$); the WRW is unstable for an even smaller range of wavenumbers (zonal wavenumbers $\gtrsim -1$). For |zonal wavenumber| $> 1$, the WRW and ERW modes propagate slower than the dry Rossby wave phase speed. The ERW propagates eastward with phase speeds between 6 and 7 m s$^{-1}$. The WRW is nearly stationary, propagating westward with phase speeds $\sim$1 m s$^{-1}$.

Why does the ERW solution only appear for a limited range of zonal wavenumbers in Fig. 2? The answer lies in the behavior of the meridional inverse-scale parameter $S_y$. This parameter is displayed as a function of zonal wavenumber in Fig. 3. The meridional decay scale for the dry waves is independent of wavenumber ($S_y = 1$), while those for the ERW and WRW show wavenumber dependence. The $S_y$ value for the ERW is positive for small zonal wavenumbers but crosses the zero line for zonal wavenumbers $\gtrsim 6$, thereby violating the meridional decay condition (31). In other words, the ERW is not equatorially trapped for scales smaller than the synoptic scale. In contrast, the $S_y$ value for the WRW increases away

TABLE 1. Reference parameter values used in numerical solutions.

| Parameter | Description | Value | Units |
|---|---|---|---|
| $c$ | Dry gravity wave speed | 50 | $\mathrm{m\ s^{-1}}$ |
| $\varepsilon_q$ | Moisture sensitivity of convection | $6^{-1}$ | $\mathrm{h^{-1}}$ |
| $\varepsilon_t$ | Temperature sensitivity of convection | $2^{-1}$ | $\mathrm{h^{-1}}$ |
| $r$ | Cloud–radiative feedback parameter | 0.2 | — |
| $m_{\mathrm{eff}}$ | Effective gross moist stability | 0.1 | — |
| $\sigma_x$ | Moistening strength associated with zonal wind | $5 \times 10^{-4}$ | $\mathrm{K\ kg\ m^{-3}}$ |
| $\sigma_y$ | Strength of the meridional moisture gradient | $9 \times 10^{-9}$ | $\mathrm{K\ kg\ m^{-4}}$ |
| $M_s$ | Gross dry stability | $3.12 \times 10^{4}$ | $\mathrm{K\ kg\ m^{-2}}$ |
| $R_d$ | Gas constant of dry air | 287.06 | $\mathrm{J\ kg^{-1}\ K^{-1}}$ |
| $\beta$ | Meridional gradient of the Coriolis parameter | $2.28 \times 10^{-11}$ | $\mathrm{m^{-1}\ s^{-1}}$ |
| $L_v$ | Latent heat of vaporization of water | $2.26 \times 10^{6}$ | $\mathrm{J\ kg^{-1}\ K^{-1}}$ |
| $c_p$ | Specific heat capacity of dry air | 1004 | $\mathrm{J\ kg^{-1}}$ |

from zero with increasing zonal wavenumber, implying an increasingly narrower meridional structure. The meridional decay condition therefore restricts the range of zonal wavenumbers that can support an equatorially trapped ERW solution in any form—stable, unstable or neutral.

The $n = 1$ WRW solution in the standard parameter regime is nearly stationary (Fig. 2c), damped for zonal wavenumbers $\lesssim -1$ (Fig. 2d), and strongly trapped near the equator (Fig. 3). The closest observed analog for the WRW is the convectively coupled $n = 1$ equatorial Rossby wave (ER). The ER propagates with phase speeds $\sim 5\ \mathrm{m\ s^{-1}}$ (Wheeler et al. 2000; Kiladis et al. 2009) and exhibits greatest spectral power over zonal wavenumbers 3–5 (Wheeler and Kiladis 1999). The WRW in the standard parameter regime therefore appears to have limited observational relevance (in contrast to the ERW). However, the WRW solution does assume increased relevance when $\sigma_x < 0$ (section 6a).

### b. Horizontal structure of the ERW

The numerical dispersion relationship in Figs. 2c and 2d shows that the ERW has the primary attributes of the observed MJO: the slow eastward phase speed and planetary scale selection. We now examine the ERW horizontal structure to check how well it corresponds with that of the observed MJO. For a given wavenumber $k$, the numerical solution for $\lambda$ from (28), the expression for $\tilde{v}_1$ from (29) and the governing

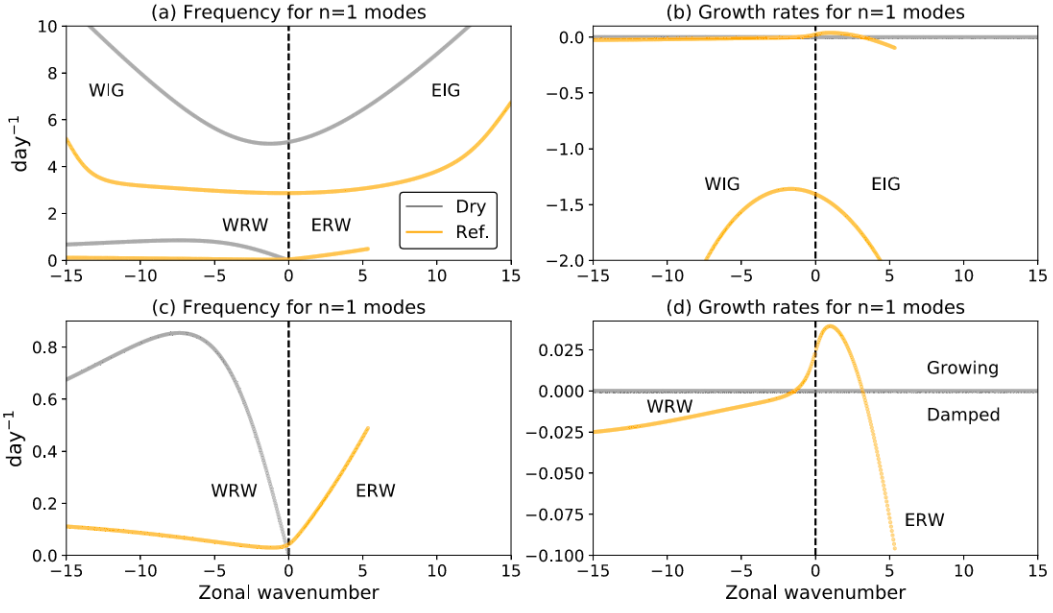


FIG. 2. (a) Wavenumber–frequency diagram for the $n = 1$ solutions in two different parameter regimes. The gray curves ("Dry") denote the dry Matsuno solutions. The orange curves ("Ref.") denote solutions obtained by numerically solving the dispersion relationship in (28), using the reference parameter values in Table 1, and then applying the meridional decay condition in (31). The solutions corresponding to the WIG, EIG, WRW, and ERW are indicated in text. (b) The growth rates for the solutions. (c),(d) Zoomed-in versions of (a) and b), respectively, that focus on the WRW and ERW solutions.

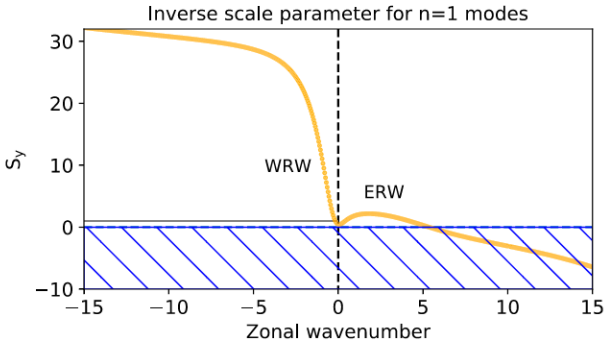


FIG. 3. The meridional inverse-scale parameter $S_y$ as defined in (30) displayed as a function of zonal wavenumber. The orange curves denote the $S_y$ values for the WRW and ERW. The gray curve denotes the $S_y$ value for the westward-propagating dry Rossby wave. The blue-hatched region indicates $S_y$ values forbidden by the condition in (31).

Eqs. (14)–(18) are sufficient to recover the horizontal structures for all the state variables (see the appendix).

### 1) CANONICAL FORM

The canonical MJO horizontal structure—as often depicted in observed composites—is roughly a zonal wavenumber-2 feature (Rui and Wang 1990; Hendon and Liebmann 1994; Kiladis et al. 2005; Adames and Wallace 2014). For ease of comparison with observations, the zonal wavenumber-2 ERW horizontal structure is therefore first examined in Fig. 4. This structure propagates eastward at 6.7 m s$^{-1}$. Each cycle of the wave shows a precipitation maximum confined to the near-equatorial region (Fig. 4a) and in-phase with a low-level convergence maximum (Fig. 4b). These maxima are flanked by a pair of off-equatorial temperature maxima to the west and another pair of off-equatorial temperature minima to the east (Fig. 4a). There also exist near-equatorial temperature extrema that are nearly in-quadrature with the precipitation. The low-level horizontal winds (Fig. 4b) are strongly zonal near the equator, and form pairs of cyclonic and anticyclonic gyres off the equator. These gyres are in-phase with the off-equatorial temperature extrema. The column-integrated moisture perturbations (Fig. 4b) are patterned like the temperature perturbations, except that the near-equatorial moisture maximum is displaced to the west of the temperature maximum. The precipitation is more in-phase with the moisture than with temperature perturbations; although there still exists a noticeable moisture–precipitation quadrature relationship.

The structure displayed in Fig. 4 is similar to that in Fig. 3 of Emanuel (2020), suggesting that the ERW is likely the same MJO-like mode reported in that study. The horizontal structure in Fig. 4 compares favorably with several observation and reanalysis based MJO composites (Rui and Wang 1990; Hendon and Salby 1994; Hendon and Liebmann 1994; Kiladis et al. 2005; Adames and Wallace 2014, 2015). For instance, the pattern of temperature and precipitation anomalies in Fig. 4a is similar to Fig. 7a of Adames and Wallace (2014). The off-equatorial gyres in Fig. 4b are a well-documented property of the MJO (e.g., Rui and Wang 1990; Hendon and Liebmann 1994; Kiladis et al. 2005). The equatorial precipitation maximum in Fig. 4 appears centered between low-level easterly and westerly maxima, similar to the Indo-Pacific warm pool composite in Adames and Wallace (2014, see their Fig. 7b).

Differences between observed MJO composites and the horizontal structure in Fig. 4 do exist, and likely arise due to structural limitations and parametric uncertainties in the model. For instance, the observed regime in which the precipitation maximum coincides with surface perturbation westerlies (Zhang and McPhaden 2000) is not captured. The small quadrature component between precipitation and column-integrated moisture is also at odds with observed

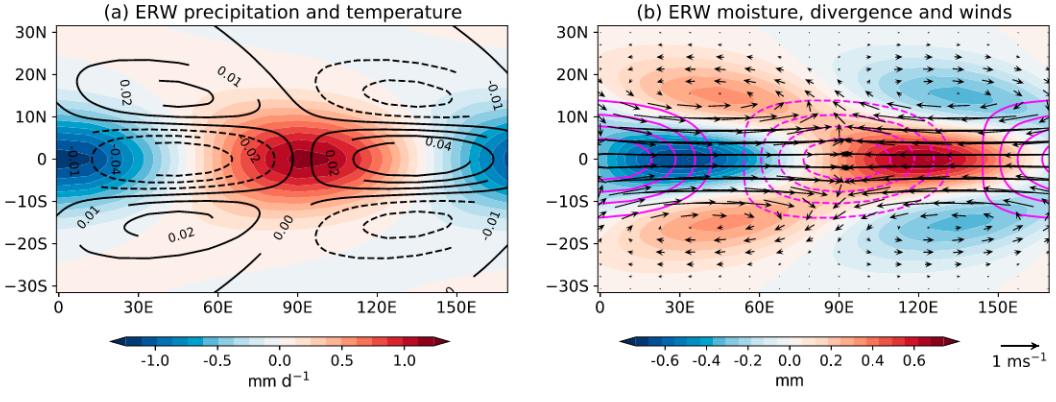


FIG. 4. The horizontal structure of the ERW for zonal wavenumber 2. The $x$ and $y$ axes values are presented in units of latitude and longitude for ease of interpretation (with the conversion factor 1° = 111 km). (a) The precipitation (colors) and column-averaged temperature (line contours). Each contour line corresponds to change in 0.01 K and the peak temperature contour is 0.04 K; negative temperature values are dashed. (b) The column-integrated moisture (colors), the low-level horizontal wind vectors (black arrows), and the low-level horizontal divergence (magenta lines). Negative divergence contours are dashed. The peak divergence contours correspond to $1 \times 10^{-6}$ s$^{-1}$, each contour line represents an interval of $0.25 \times 10^{-6}$ s$^{-1}$. The 1 m s$^{-1}$ reference wind vector is provided; the peak zonal wind vector corresponds to 5 m s$^{-1}$.

MJO composites (e.g., Kim et al. 2014; Adames and Wallace 2015), which instead show these quantities to be nearly in-phase. Possible reasons for this discrepancy as discussed in section 7a. Another example is the relative strength of the equatorial versus off-equatorial temperature perturbations. In Fig. 4, the equatorial temperature perturbations appear stronger than off-equatorial perturbations—in contrast to some observed composites (e.g., Hendon and Liebmann 1994). However, this discrepancy diminishes when considering slightly different parameter regimes (Fig. S2 in the online supplemental material).

Overall, the zonal wavenumber-2 ERW appears to possess the phase speed, planetary-scale selection, and much of the observed horizontal structure of the MJO. This strongly suggests that the ERW is a beta-plane analog of the MJO. The ERW horizontal structure in Fig. 4 is sometimes interpreted as a coupled Kelvin–Rossby pattern (Rui and Wang 1990; Wang and Li 1994; Kang et al. 2013; Wang and Chen 2017). This interpretation is motivated by apparent similarities with the steady-state response to equatorial heating (Gill 1980). Figure 4 highlights that such structures can also be eigenfunctions in their own right, and arise from ERW modes that are distinct from both the equatorial Kelvin wave and the WRW.

#### 2) Zonal wavenumber dependence

In the standard parameter regime, the canonical MJO horizontal structure—with equatorial convergence and off-equatorial gyres—is well-captured by the zonal wavenumber-2 ERW. However, this structure is not fixed, but varies with model parameters. Figure 5 depicts the sensitivity of the ERW horizontal structure to zonal scale. The zonal wavenumber-1 horizontal structure is displayed in Figs. 5a and 5b. This structure corresponds to the most unstable ERW solution (Fig. 2d). A prominent equatorial convergence center and strong meridional tilts in temperature perturbations characterize the zonal wavenumber-1 ERW (Fig. 5a). The wind perturbations in Fig. 5b—that must balance the temperature perturbations—are nearly zonal everywhere. The off-equatorial gyres are consequently weaker in Fig. 5b, when compared to Fig. 4b. As the zonal wavenumber increases, the meridional tilt in the temperature structure reduces (Figs. 5c,e,g). This reduction is coincident with increasingly prominent off-equatorial gyres (Figs. 5d,f,h). Figure 5 thus demonstrates that while strong equatorial convergence is a robust feature of the ERW (in the standard parameter regime), the strength of the accompanying off-equatorial gyres can vary with zonal scale.

## 5. Phase speeds and scale selection for the ERW

### a. The ERW as a QE mode

Preliminary insight into ERW dynamics is obtained by simply computing the ratio of peak moisture to temperature perturbations (both with units of K kg m$^{-2}$) from Fig. 4. This ratio is ~3.6, and is close to the ratio of $\varepsilon_f/\varepsilon_q$ (=3). This suggests that the ERW is closer to being a convective quasi-equilibrium (QE) mode than a moisture mode (A21). It was shown in A21 that QE modes have leading-order thermodynamic properties strongly constrained by the convective adjustment process. In contrast, moisture modes have leading-order thermodynamics constrained by gravity wave adjustment, and possess larger moisture-temperature ratios ($\gg\varepsilon_f/\varepsilon_q$). This QE versus moisture mode classification of the ERW provides useful context when examining the mechanisms governing the mode phase speed and scale selection.

### b. Dispersion relationship

Analytic approximations for the ERW and WRW dispersion curves in Fig. 2 are now sought. The following nondimensional parameters are first defined:

$$m_r = m_{\text{eff}}\frac{\varepsilon_q}{\varepsilon_a}, \tag{32}$$

$$\eta_x = \xi_x\frac{(1+r)}{m_{\text{eff}}k}, \tag{33}$$

$$\eta_y = \xi_y\frac{(1+r)c}{m_{\text{eff}}\beta}. \tag{34}$$

The parameter $m_r$ is the reduced gross moist stability (A21). This parameter captures the reduction in the effective gross moist stability due to differences between the moisture sensitivity ($\varepsilon_q$) and the effective adjustment time scale ($\varepsilon_a$) of convection. The parameters $\eta_x$ and $\eta_y$ are nondimensionalized versions of $\xi_x$ and $\xi_y$, respectively. In (33) and (34), measures of the zonal scale ($k^{-1}$) and the meridional scale ($\sqrt{c/\beta}$) appear as relevant normalizing factors. Two additional variants of $m_r$ are now introduced:

$$m_{r1} = n(n+1)m_r\eta_y, \tag{35}$$

$$m_{r2} = m_r[(1+m_{r1}\eta_y)(1+i\eta_x)+n(n+1)\eta_x^2]. \tag{36}$$

Both $m_{r1}$ and $m_{r2}$ are forms of $m_r$ that incorporate the effects of the meridional moisture advection ($\eta_y$), the moistening due to zonal wind ($\eta_x$) and the meridional mode $n$. With these parameters defined, an analytic dispersion relationship for both the ERW and WRW is obtained (see derivation in the appendix):

$$\lambda = ck\left(\frac{m_{r1}\eta_x - i[2m_{r1}\pm(2n+1)\sqrt{m_{r2}}]}{(2n+1)^2+m_{r1}\eta_y}\right)+O(k^2). \tag{37}$$

The above expression is valid in the limit of $k\to 0$ and for finite $m_{\text{eff}}$ values; the higher-order terms are denoted by $O(k^2)$. The two solutions given by plus and minus signs in the numerator of (37) denote the ERW and WRW modes, respectively. This algebraic connection further supports the interpretation that the ERW is an eastward-propagating counterpart of the WRW.

Removing the moistening effects by perturbation winds ($\eta_x=\eta_y=0$) and setting $m_r=1$ (for a dry atmosphere) in the WRW solution from (37) yields the dispersion relationship for the dry, long Rossby wave: $\lambda = ick/(2n+1)$. This shows that the WRW is indeed a moist version of the dry Rossby wave. Setting $n=-1$ in the WRW solution yields the moist, long Kelvin wave dispersion relationship: $\lambda = -ick\sqrt{m_r(1+i\eta_x)}$—see Eq. (26) in

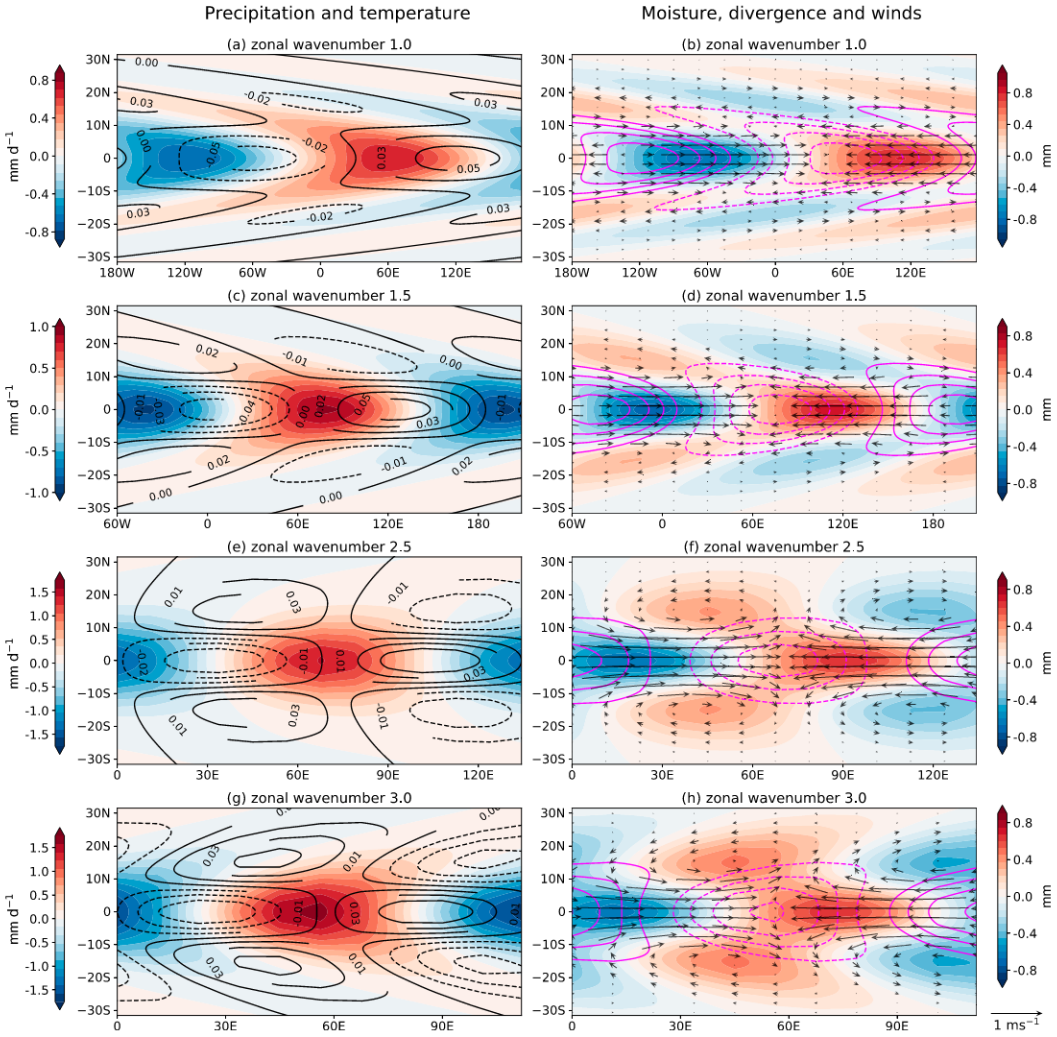


FIG. 5. As in Fig. 4, but for zonal wavenumbers (a),(b) 1; (c),(d) 1.5; (e),(f) 2.5; and (g),(h) 3. The peak divergence (magenta) contours correspond to (b) $\pm 0.6 \times 10^{-6}$, (d) $\pm 0.8 \times 10^{-6}$, and (f),(h) $\pm 1.2 \times 10^{-6}\,\mathrm{s}^{-1}$. The magenta contour lines have intervals of (b) $0.15 \times 10^{-6}$, (d) $0.2 \times 10^{-6}$, and (f),(h) $0.4 \times 10^{-6}\,\mathrm{s}^{-1}$. The peak zonal wind vector in each case corresponds to $5\,\mathrm{m\,s}^{-1}$.

A21. Similarly, the $n = -1$ version of the ERW solution is the westward-propagating, spurious "anti-Kelvin" wave with dispersion relationship: $\lambda = ick\sqrt{m_r(1 + i\eta_x)}$.

The leading-order analytic frequencies and growth rates follow from (37) as $\mathrm{Re}[\lambda]$ and $-\mathrm{Im}[\lambda]$, respectively, where $\mathrm{Im}[\cdots]$ denotes the imaginary component. These analytic versions are compared to the corresponding numerical solutions in Fig. 6. The longwave frequencies for both the WRW and ERW in Fig. 6a are nearly linear in $k$ and are therefore well-captured by the analytic expression in (37) for zonal wavenumbers with absolute values <5. On the other hand, the growth rates—particularly for the ERW in Fig. 6b—have strong higher-order contributions. The first-order solution in (37) is therefore only valid in a narrow zonal wavenumber range (absolute values <1). The dispersion relationship in (37) can be extended to include the $O(k^2)$ component and thereby obtain a better correspondence to the numerical solutions in Fig. 6b. However, the $O(k^2)$ extension is too unwieldy to mine for physical insights and is not introduced here. For our purposes, it is sufficient to note that the $O(k^2)$ term is a scale-selector for the ERW that preferentially damps the shortwave solutions.

The leading-order ERW and WRW phase speeds are now given by

$$-\mathrm{Im}\left[\frac{\lambda}{k}\right] = \underbrace{c\frac{2m_{r1}}{(2n+1)^2 + m_{r1}\eta_y}}_{c_a} \pm \underbrace{c\frac{(2n+1)\mathrm{Re}[\sqrt{m_{r2}}]}{(2n+1)^2 + m_{r1}\eta_y}}_{c_{\mathrm{gms}}}. \quad (38)$$

In the above expression, we take the principal square root such that $\mathrm{Re}[\sqrt{m_{r2}}] \geq 0$. According to (38), the ERW and WRW phase speeds have two additive contributors: $c_a$ and $c_{\mathrm{gms}}$. The term $c_a$ is nonzero only in the presence of a meridional moisture

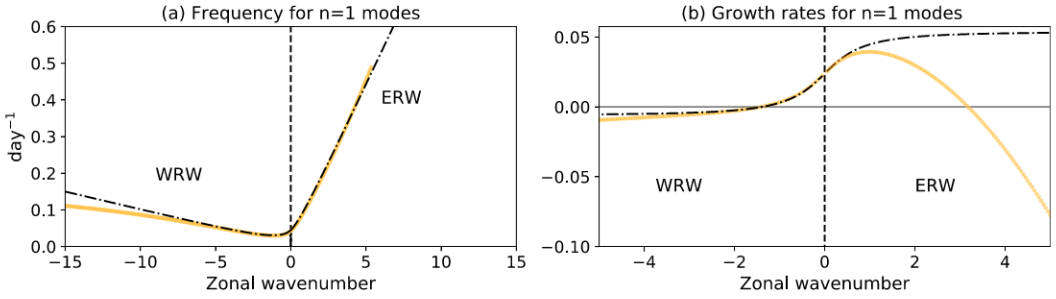


FIG. 6. As in Figs. 2c and 2d, but only for the ERW and WRW. The orange curves are the numerical solutions. The dashed–dotted lines are obtained from the analytic approximation in (37). Note differences in $x$-axis range between (a) and (b).

gradient. Since $\eta_y > 0$, we see that this term induces eastward propagation in both the ERW and WRW. For zonal wavenumber 2, $c_a$ contributes an eastward phase speed of $\sim 2.9\,\mathrm{m\,s^{-1}}$. We posit that this eastward propagation arises due to meridional advection moistening to the east of the low-level cyclonic gyres in Fig. 4b. The term $c_a$ thus contributes to the "inverse beta effect" by countering the effects of the planetary vorticity gradient (Sobel et al. 2001; Sukhatme 2014; Hayashi and Itoh 2017).

For zonal wavenumber 2, the term $c_{\mathrm{gms}}$ in (38) contributes an eastward phase speed of $\sim 4.0\,\mathrm{m\,s^{-1}}$ for the ERW, and the same westward phase speed for the WRW. This term plays an equivalent role to that of gross moist stability in tropical wave propagation. Long, convectively coupled tropical waves propagate slower than dry waves due to a reduction in the static stability (Emanuel et al. 1994; Neelin and Yu 1994; Tian and Ramanathan 2003; Haertel and Kiladis 2004; Frierson 2007; Raymond et al. 2009; Powell 2017). In a simpler system, this reduction is captured by $m_r$ or more precisely, the phase speeds $\sim c\sqrt{m_r}$ (A21). For the ERW and WRW, this phase speed reduction is captured by $c_{\mathrm{gms}}$. This is made clear by zeroing out the moistening effects of meridional and zonal winds ($\eta_x = \eta_y = 0$) in (38) upon which $c_a$ vanishes, and $c_{\mathrm{gms}}$ reduces to $c\sqrt{m_r}$. It is worth noting that a reduced phase speed due to a small gross moist stability is a signature of QE modes.

Figure 6b shows that the ERW is unstable near planetary scales due to the $O(k)$ term in (37). The leading-order growth rates implied by this term are

$$\mathrm{Re}[\lambda] = ck\left(\frac{m_{r1}\eta_x}{(2n+1)^2 + m_{r1}\eta_y} \pm \frac{(2n+1)\mathrm{Im}[\sqrt{m_{r2}}]}{(2n+1)^2 + m_{r1}\eta_y}\right), \quad (39)$$

where the plus and minus signs denote the growth rates for the ERW and WRW, respectively. It can be verified that for the ERW, both the terms in (39) are positive when $\sigma_x > 0$, and negative when $\sigma_x < 0$. Therefore, a necessary condition for positive ERW growth rates at planetary scales is that low-level easterly perturbation winds moisten the column ($\sigma_x > 0$).

### c. Moist static energy budgets

The expression in (39), though useful, does not indicate why the ERW growth rates must *maximize* near planetary length scales. Column-integrated moist static energy (MSE) budgets are now employed to probe this question. This approach has been widely used to understand mechanisms associated with the growth as well as propagation of the tropical disturbances (Back and Bretherton 2006; Maloney 2009; Kiranmayi and Maloney 2011; Andersen and Kuang 2012; Arnold et al. 2015; Wolding and Maloney 2015; Inoue and Back 2015, among many others).

We begin by adding the temperature and moisture budgets, (5) and (6), and following the same reduction procedures from section 2 to obtain the MSE budget:

$$\frac{\partial\langle h\rangle}{\partial t} = \omega_1 m M_s + \sigma_x u_1 - \sigma_y y v_1 + \langle Q_r\rangle, \quad (40)$$

where $\langle h\rangle = \langle T\rangle + \langle q\rangle$ is the MSE measure for our system—since baroclinic geopotential perturbations vanish upon column integration. It has been verified that the MSE budget in (40) is closed for the ERW. This serves as a consistency check that the numerical solutions from the root solver do indeed satisfy the governing equations.

A prognostic equation for the domain-wide perturbation MSE amplitude is constructed by multiplying (40) by $\langle h\rangle$ and integrating over the domain:

$$\frac{\partial}{\partial t}\left\{\frac{|\langle h\rangle|^2}{2}\right\} = mM_s\{\omega_1\langle h\rangle\} + \sigma_x\{u_1\langle h\rangle\} - \sigma_y\{yv_1\langle h\rangle\} + \{\langle Q_r\rangle\langle h\rangle\}, \quad (41)$$

where the curly braces $\{\cdots\}$ denote a double integration across the zonal and meridional directions. The left-hand side of (41) is positive for unstable disturbances and negative for stable disturbances. The terms on the right-hand side of (41) quantify the contribution of each term to disturbance growth or decay. The numerical version of the double integration operation is computed as a double summation normalized by a measure of the MSE perturbation strength (as in Andersen and Kuang 2012; Arnold et al. 2015). For example, the term $\{\langle Q_r\rangle\langle h\rangle\}$ is computed as

$$\{\langle Q_r\rangle\langle h\rangle\} = \frac{\sum_{y=y_s}^{y_n}\sum_x \langle Q_r\rangle\langle h\rangle}{\sum_{y=y_s}^{y_n}\sum_x \langle h\rangle^2}, \quad (42)$$

and similarly for other terms in (41). Here $y_n$ and $y_s$ are the meridional extents of the domain and are taken to be $\pm 5000$ km.

The normalization in (42) ensures units of inverse time, which allows a comparison with $\lambda$.

Figure 7 shows the horizontal structures of the MSE source terms from (40) for the zonal wavenumber-2 ERW. The dominant off-equatorial MSE term is clearly meridional moisture advection ($-\sigma_y y v_1$). Comparing Fig. 7a to Fig. 4b shows that positive meridional moisture advection maximizes to the east of the low-level cyclonic gyres, as expected from the poleward flow acting on the meridional moisture gradient. This moistening likely contributes to the eastward propagation of the ERW, as implied by $c_a$ in (38). Near the equator, the dominant MSE terms are the moistening effects due to zonal wind ($\sigma_x u_1$), vertical MSE advection ($\omega_1 m M_s$) and radiative heating $\langle Q_r \rangle$. The $\sigma_x u_1$ term maximizes to the east of the convergence center, within the region of strong near-equatorial easterlies seen in Fig. 4b. The $\omega_1 m M_s$ term (Fig. 7b) is almost exactly out-of-phase with the near-equatorial precipitation (Fig. 4a); whereas $\langle Q_r \rangle$ is (by definition) in-phase with the near-equatorial precipitation.

Figure 7c shows the "growth budget" for the zonal wavenumber-2 ERW. This is computed by applying the double summation operator defined in (42) to every term in (41). The largest positive contributor to ERW MSE growth is the radiative heating $\langle Q_r \rangle$. This contribution is opposed by the damping effects due to vertical MSE advection ($\omega_1 m M_s$)—also seen in Fig. 7b. The moisture transports by zonal ($\sigma_x u_1$) and meridional ($\sigma_y y v_1$) winds also contribute to ERW growth. From the MSE budget perspective, the zonal wavenumber-2 ERW is unstable because within precipitating regions, MSE import by radiative heating, and the moistening effects of zonal and meridional winds are sufficient to overcome the MSE export by vertical advection.

One level of explanation for the ERW planetary scale-selection is available from a growth budget over the near-equatorial region ($|y| < 1000$ km). This narrowed analysis separates the dynamics associated with equatorial convergence center from the off-equatorial gyres of the ERW. Figure 8 shows the near-equatorial ERW MSE growth budget as a function of zonal wavenumbers from 1 to 4. This is the range over which the ERW growth rates go from positive to negative in Fig. 6b. The meridional extent of the summation in (42) is restricted to $\pm 1000$ km. The decrease in MSE growth (orange bars) with increasing zonal wavenumber in Fig. 8 tracks the corresponding change in ERW growth rates over the same wavenumber range in Fig. 6b, justifying the focus on the near-equatorial growth budget. The radiative heating—a large MSE source—is always out-of-phase with vertical MSE advection—a large MSE sink. There consequently exists significant cancellation between these terms (Fig. S3 in the online supplemental material). Furthermore, the radiative heating can be expressed as a fixed proportion of the vertical MSE advection (Fig. S4 in the online supplemental material). Only the sum of vertical MSE advection and radiative heating is therefore shown in Fig. 8.

As the ERW zonal scale decreases, the damping due to the vertical MSE advection term becomes increasingly stronger than the positive contributions from radiative heating. The moistening due to the zonal winds (blue bars) is also less effective with decreasing scale. The meridional moisture advection (magenta bars) contributes more to ERW perturbation growth at shorter scales, but this contribution is insufficient to prevent the mode damping. Overall, Fig. 8 suggests that at the largest horizontal scales and within near-equatorial precipitating columns, vertical advection is least effective at exporting MSE, while the moistening effects of zonal winds are most effective in importing MSE. A combination of these two effects maximizes ERW growth at the largest scales.

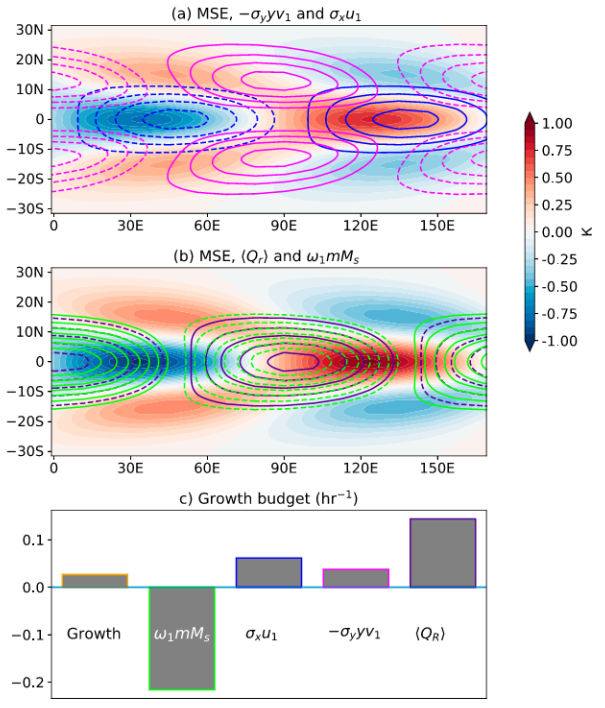


FIG. 7. (a),(b) MSE (color) and the MSE budget terms (line contours) from (40) for the zonal wavenumber-2 ERW. The terms are presented as column averages after normalizing (40) over a column pressure depth of 800 hPa. The line contours in (a) show terms $\sigma_x u_1$ (blue) and $-\sigma_y y v_1$ (magenta), while those in (b) show terms $\langle Q_r \rangle$ (purple) and $\omega_1 m M_s$ (green). Negative line contours are dashed. The contour lines are spaced $10^{-3}$ K h$^{-1}$ apart in (a) and $2 \times 10^{-3}$ K h$^{-1}$ apart in (b). The peak values for both magenta and blue contours are $\pm 4 \times 10^{-3}$ K h$^{-1}$ in (a). The peak values are $\pm 10^{-2}$ and $\pm 1.4 \times 10^{-2}$ K h$^{-1}$ for the purple and green contours, respectively, in (b). (c) The growth budget terms for the zonal wavenumber-2 ERW computed using (41) and (42).

The increasing damping efficiency of vertical MSE advection with wavenumber is a form of moist convective damping (MCD; Emanuel 1993; Yu and Neelin 1994; Emanuel et al. 1994). This phenomenon arises due to the finiteness of the convective adjustment time scale and acts on all QE modes (Yu and Neelin 1994). When $k \to 0$, the near-equatorial moisture and temperature anomalies are in-phase, and are both nearly in quadrature with the precipitation and $\omega_1$ (e.g., see Figs. 5a,b). This is also the limit of strict QE that can be enforced at any wavenumber with instantaneous convective adjustment. In this limit, the damping due to vertical MSE advection or $mM_s\{\omega_1 \langle h \rangle\}$ approaches zero due to the quadrature relationship between $\omega_1$

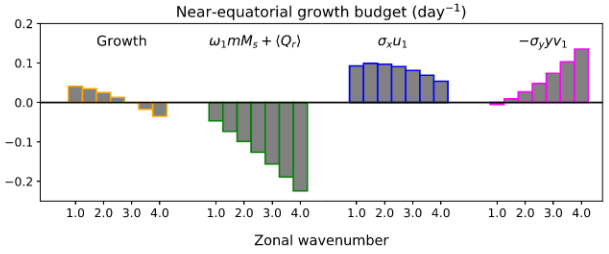


FIG. 8. The near-equatorial MSE growth budget for zonal wavenumbers 1–4. Each budget term is shown as function of wavenumber with intervals of 0.5.

and $\langle h \rangle$. As $k$ increases away from zero, the moisture anomalies—which dominate the MSE anomalies—get less in-phase with temperature, and more in-phase with precipitation (and more out-of-phase with $\omega_1$). This change in the precipitation–moisture–temperature phase relationship with $k$ is also visible in Fig. 5. With increasing $k$, the damping by $\omega_1 mM_s$ is therefore more efficient due to the increasing out-of-phase relationship between $\omega_1$ and $\langle h \rangle$.

The changing $\omega_1$–$\langle h \rangle$ phase relationship with wavenumber also plays a role in the diminished influence of $\sigma_x u_1$ at smaller scales. We observe that $\sigma_x u_1$ has the largest magnitude (Fig. 7b) in the near-equatorial region where the winds are almost purely zonal (Fig. 4b). We therefore insert $v_1 = 0$ in (16) to obtain

$$\{u_1 \sigma_x \langle h \rangle\} = \frac{\sigma_x}{k} \{i\omega_1 \langle h \rangle\}. \tag{43}$$

In the limit of $k \to 0$ (or strict QE), $i\omega_1$ and $\langle h \rangle$ are nearly in-phase for eastward-propagating disturbances. Therefore, $\sigma_x u_1$ supports the growth of eastward-propagating disturbances (provided $\sigma_x > 0$). Two effects arise as $k$ increases away from zero. In the first effect, the $i\omega_1$–$\langle h \rangle$ relationship changes from being in-phase to more in quadrature. The $\{i\omega_1 \langle h \rangle\}$ term consequently decreases from a positive value toward zero as the zonal scale gets smaller. In the second effect, the perturbation zonal winds weaken due to the $k^{-1}$ factor in (43). A combination of both the changing phase difference between $\omega_1$ and $\langle h \rangle$, and weakening zonal winds makes the $\sigma_x u_1$ term less efficient at smaller scales.

Broadly speaking, both MCD and the moistening effects due to zonal wind act as scale selectors for the ERW. However, the ERW scale selection is also shaped by other factors such as the meridional tilt in the horizontal structures. These additional factors are required to explain why the ERW growth rates maximize at a wavenumber slightly greater than zero (Fig. 6b). This level of explanation is more involved and is therefore deferred until further study.

## 6. Parameter perturbations

We now briefly explore the parameter space for valid ERW solutions, and thereby identify optimal background states for this mode. The dispersion relationship in (37) suggests that the ERW properties are sensitive to the moistening strength associated with zonal winds ($\sigma_x$), the meridional moisture gradient parameter ($\sigma_y$), the effective gross moist stability ($m_{\text{eff}}$) and the meridional mode $n$. A set of perturbation experiments are accordingly carried out for these parameters. For $\sigma_x$, $\sigma_y$ and $m_{\text{eff}}$, the corresponding reference values from Table 1 are perturbed with a set of multipliers. For the meridional mode, solutions are shown for integer values of $n$ from 0 to 4.

### a. *Varying $\sigma_x$, $\sigma_y$, and $m_{eff}$*

Figure 9 show the sensitivity of the ERW and WRW solutions to changes in $\sigma_x$. The reference $\sigma_x$ parameter is perturbed with a series of multipliers from −0.25 to 2 in steps of 0.25. The ERW remains a valid solution at small zonal wavenumbers through this range of $\sigma_x$ values. From Fig. 9a it is seen that the ERW and WRW frequencies are only weakly sensitive to $\sigma_x$. This property is also reflected in the phase speeds for the zonal wavenumber-2 ERW (Fig. 9c), which vary within a narrow range of 6.5–7.5 m s$^{-1}$. In contrast, the ERW growth rates are more sensitive to $\sigma_x$ (Fig. 9b); both the maximum growth rate and the wavenumber of maximum growth increase with $\sigma_x$. Figure 9 shows that the ERW exists even without zonal wind–dependent moistening ($\sigma_x = 0$) or when moistening is associated with perturbation westerlies ($\sigma_x < 0$). The ERW modes are either neutral or damped when $\sigma_x \leq 0$. The parameter range $\sigma_x < 0$ can be equivalently interpreted as one with strong basic-state surface westerlies or a negative background zonal moisture gradient or both. When $\sigma_x < 0$, the WRW is unstable at planetary scales while the ERW is damped—as seen from the inset within Fig. 9b. The dependence on the sign of $\sigma_x$ might explain why westward-propagating modes are favored over eastward modes when the near-equatorial zonal moisture gradient is reversed (Gonzalez and Jiang 2019). Note that the unstable WRW solution from the Fig. 9b inset does not quite match the phase speed and scale of the westward-propagating disturbances documented in Gonzalez and Jiang (2019). However, the background state dependent *preference* for eastward versus westward intraseasonal modes is qualitatively captured.

Figure 10 explores the sensitivity of the solutions to the strength of the meridional moisture gradient $\sigma_y$. This parameter is perturbed similarly to $\sigma_x$ except that negative values are omitted. For smaller values of $\sigma_y$ (<0.75 times the reference value), the ERW is not a valid solution to the governing equations. A threshold meridional moisture gradient is therefore a necessary condition for the ERW to exist when $m_{\text{eff}} > 0$.

The zonal wavenumber-2 ERW phase speed generally increases with $\sigma_y$ (Fig. 10c). This conforms to the earlier interpretation—using $c_a$ in (38)—that when meridional moisture gradients are stronger, advection is more effective at propagating moisture anomalies. Changes in $\sigma_y$ can arise from changes to the meridional structure of the sea surface temperature (SST). The dependence of the ERW phase speeds on $\sigma_y$ is generally consistent with modeling studies (Kang et al. 2013; Jiang et al. 2020) that report slower eastward propagation speeds with a broader meridional SST distribution.

As $\sigma_y$ increases, the range of wavenumbers supporting a valid ERW solution also widens. For example, in Fig. 10a

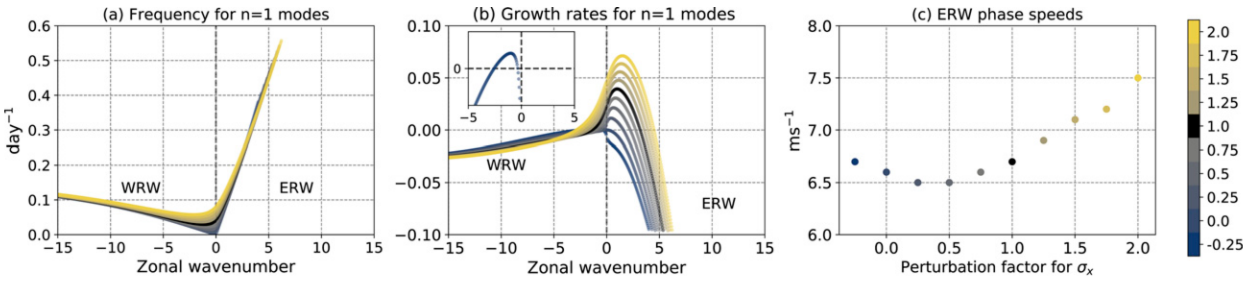


FIG. 9. (a) Frequencies and (b) growth rates obtained from the $\sigma_x$ perturbation experiment. (c) Phase speeds for the zonal wavenumber-2 ERW as a function of the $\sigma_x$ perturbation factor. The colors denote the different perturbation factors whose values are indicated in the color bar. A perturbation factor of 1 denotes the standard reference run and is colored black. The inset in (b) shows the solution with $\sigma_x < 0$ for zonal wavenumbers near 0.

when $\sigma_y$ is twice the reference value, the valid range extends to zonal wavenumber ~11. For this $\sigma_y$ value, the ERW frequencies show a transition around wavenumber 4. This transition marks a sharp departure from the leading-order linear approximation in (37). Around the same wavenumber, the scale selective damping in the growth rates transitions to scale-independent damping. This damping rate asymptotes to a value of $-m_{\text{eff}}\varepsilon_q$ (the red dashed line in Fig. 10b). Since $\lambda = -m_{\text{eff}}\varepsilon_q$ is the moisture mode growth rate (Sobel et al. 2001; Sugiyama 2009; Adames et al. 2019, A21), we infer that this qualitative change in the ERW solution marks the QE–WTG transition (A21). This transition further contrasts the longwave ERW solution (which are QE modes) from shortwave moisture modes. The moisture modes do not show scale-selective damping because of the absence of MCD, and negligible contributions to mode growth from zonal wind-driven moistening at short wavelengths.

The results from the $m_{\text{eff}}$ perturbation experiments are shown in Fig. 11. Here, $m_{\text{eff}}$ is perturbed similarly to $\sigma_y$, except that an additional solution is shown for a perturbation factor of 0.125 to better resolve the changes as $m_{\text{eff}} \to 0$. The ERW is a valid solution for the range of $m_{\text{eff}}$ values explored here. As $m_{\text{eff}} \to 0$, discontinuities in the solutions and QE–moisture mode transitions appear. When $m_{\text{eff}}$ is 0.25 times the reference value, a jump discontinuity is seen in the frequency curve (Fig. 11a). The shortwave growth rate (Fig. 11b) to the right of this jump asymptotes to a value of $-m_{\text{eff}}\varepsilon_q$; this jump therefore marks the QE–moisture mode transition. When $m_{\text{eff}} = 0.0125$ (or 0.125 times the reference value), the jump discontinuity is replaced by a continuous curve; the QE–moisture mode transition wavenumber is now marked by a kink in the frequency curve (Fig. 11a). With decreasing $m_{\text{eff}}$, the maximum ERW growth rate increases (Fig. 11b) and zonal wavenumber-2 ERW phase speed decreases (Fig. 11c). For the perturbed $m_{\text{eff}}$ values, the phase speeds in Fig. 11c range between ~4–8 m s$^{-1}$. Furthermore, the phase speeds in Fig. 11c scale like $\sqrt{m_{\text{eff}}}$, pointing to an influence from term $c_{\text{gms}}$ in (38). This phase speed scaling is another property of QE modes (A21).

The $m_{\text{eff}} = 0$ solution is similar to that with $m_{\text{eff}} = 0.0125$, except that the former case has a smaller wavenumber range with valid ERW solutions. In Fig. 11b, two anomalous features are noted for the $m_{\text{eff}} = 0$ case. The first is the discontinuity within the WRW solution for negative planetary-scale wavenumbers. The second is that the shortwave ERW growth rate asymptotes to a value less than zero; this differs from the anticipated asymptotic moisture mode growth rate for this case (which is zero). A better understanding of the $m_{\text{eff}} = 0$ case can be pursued by obtaining analytic dispersion relationships—similar to (37)—in the limit of $m_{\text{eff}} \to 0$.

The pertinent conclusion from the $m_{\text{eff}}$ perturbation experiments is that a valid ERW solution only exists when $m_{\text{eff}} \gtrsim 0$ and $m_{\text{eff}} \lesssim 0.25$. Neither large negative $m_{\text{eff}}$ values—corresponding to unstable background states—nor large positive $m_{\text{eff}}$ values—corresponding to dry background states—apparently support an ERW solution in the presence of a background meridional moisture gradient. Interestingly, eastward-propagating $n = 1$ modes do emerge without a

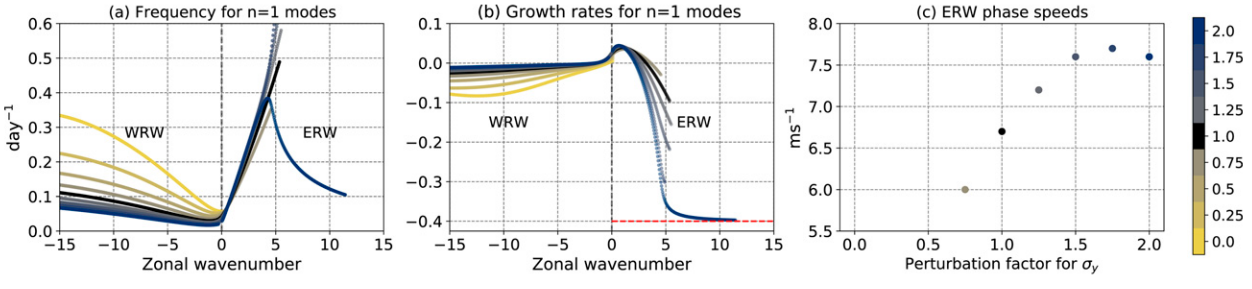


FIG. 10. As in Fig. 9, but for $\sigma_y$ perturbation experiments. The red dashed horizontal line in (b) is the moisture mode growth rate (see text).

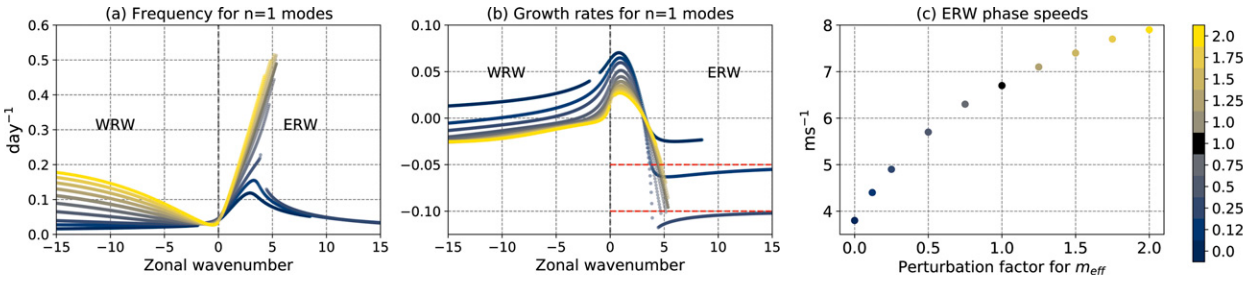


FIG. 11. As in Fig. 9, but for $m_{\text{eff}}$ perturbation experiments. The red horizontal dashed lines in (b) denote moisture mode growth rates.

meridional moisture gradient ($\sigma_y = 0$) and when $m_{\text{eff}} < 0$ (Fig. S6 in the online supplemental material).

### b. Varying the meridional mode

All permissible solutions for integer values of $n$ from 0 to 4 are shown in Fig. 12. The Kelvin wave solution is also included for completeness; this solution is obtained by solving the $v = 0$ system from A21 using the parameter set in Table 1. When $n = 0$, there are no ERWs. As in the dry case, the only valid $n = 0$ solutions are the westward-propagating mixed Rossby–gravity wave (MRG) and the EIG. When $n > 0$, WIGs, EIGs, WRWs, and ERWs emerge as permissible solutions. The EIGs and WIGs for the different meridional modes are well separated in both the frequency (Fig. 12a) and the growth rates (Fig. 12b). The $n = 1$ WRW also appears separated from the higher-order WRW modes. In contrast, the different meridional modes of the ERW have nearly the same dispersion curves, with strong overlap in the frequencies (Fig. 12c) and only slight differences in the growth rates (Fig. 12d). The higher-order ERW meridional modes are valid solutions over a slightly extended range of wavenumbers. The Kelvin wave solution shown in Fig. 12 corresponds to the "propagating deep convective mode" of Neelin and Yu (1994) and the "WISHE moisture mode" of Fuchs and Raymond (2017). The frequency curve for this solution (Fig. 12c) displays a kink near zonal wavenumber 6 marking the QE–moisture mode transition (A21). Interestingly, the Kelvin wave solution occupies the same wavenumber–frequency space as the ERW (Fig. 12c), and shows similar growth rates (Fig. 12d) at planetary scales. These similarities raise the question of whether the Kelvin wave solution is simply the $v \to 0$ limit of the ERW solution.

## 7. Discussion

### a. Relevance for the MJO

The $n = 1$ ERW has the primary properties ascribed to the observed MJO over the Indo-Pacific warm pool: slow, eastward propagation with respect to mean flow, planetary scale selection, and a horizontal structure typically referred to as the swallow-tail (Zhang and Ling 2012) or the coupled Kelvin–Rossby pattern (Wang and Rui 1990) with quadrupole vortices (Majda and Stechmann 2009).

Additionally, the properties of the $n = 1$ ERW—like the observed MJO—are sensitive to details of the background

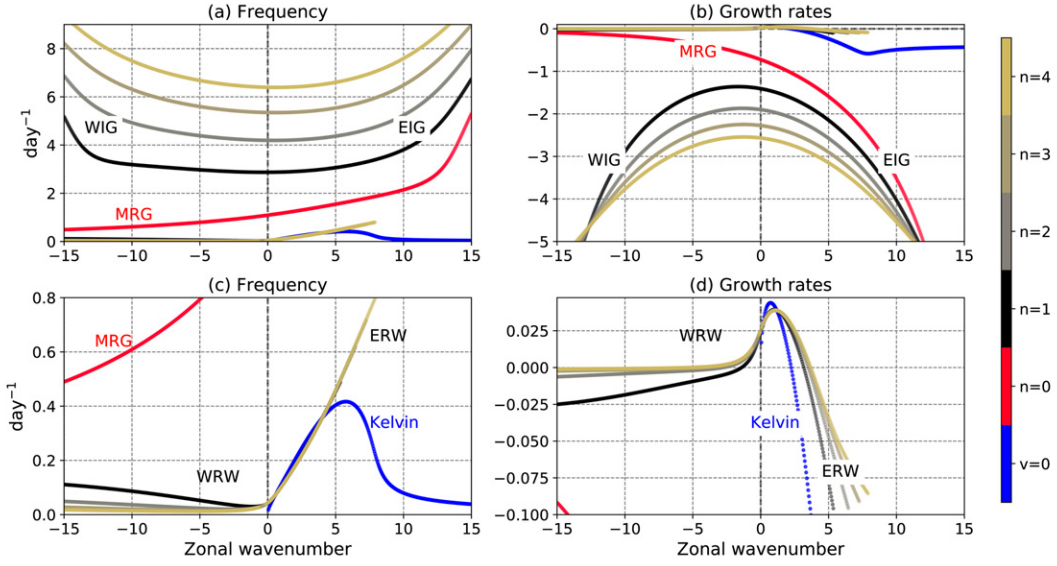


FIG. 12. As in Fig. 2, but—as indicated in the color bar—with different values for the meridional mode $n$, and including the $v = 0$ case. The westward-propagating $n = 0$ solution is the MRG (red), and the eastward-propagating $v = 0$ solution is the Kelvin wave (blue).

meridional moisture gradient. The derived dispersion relationship for the ERW suggests a leading-order contribution to the phase speed from meridional moisture advection by perturbation winds. Similar links between MJO propagation and meridional moisture advection have been advanced in reanalysis and modeling studies (Jiang et al. 2016; Gonzalez and Jiang 2017; Kim et al. 2017; DeMott et al. 2019). When the effective gross moist stability is positive, the $n = 1$ ERW only exists for meridional moisture gradients stronger than a threshold value. This existence property mirrors the results from Jiang et al. (2020), who report diminishing intraseasonal eastward-propagating variance with smaller meridional moisture gradients.

The ERW growth rate—and the phase speed to a lesser extent—is sensitive to the strength of the moistening induced by zonal wind perturbations. This strength is specified through a single parameter $\sigma_x$. By design, $\sigma_x$ does not distinguish between the different sources of zonal wind–induced moistening: surface fluxes, zonal moisture advection or some combination thereof. While the ERW can exist when $\sigma_x = 0$, it is only destabilized for $\sigma_x > 0$. This dependence might explain why either a positive zonal moisture gradient or the WISHE mechanism can excite MJO-like modes in idealized modeling experiments (Khairoutdinov and Emanuel 2018; Shi et al. 2018). When $\sigma_x < 0$, the background state is such that low-level perturbation westerlies moisten the column. Two examples of such basic states include those with (i) a negative zonal moisture gradient or (ii) strong background westerlies. Such basic states excite WRWs and damp ERWs. This parameter regime could potentially explain the connections between mean state and the preferred (eastward vs westward) mode of intraseasonal variance (Gonzalez and Jiang 2019; Jiang et al. 2020).

While the ERW growth rates are sensitive to $\sigma_x$, column-integrated radiative heating is the largest MSE source within precipitating regions. This property is qualitatively similar to that seen in the MSE budgets of the MJO (Maloney 2009; Maloney et al. 2010; Andersen and Kuang 2012; Arnold et al. 2015; Ren et al. 2021). The vertical MSE advection is a large sink term in the ERW MSE budget as for MJO MSE budgets from reanalysis data (Kiranmayi and Maloney 2011; Kim et al. 2014; Ren et al. 2021). The contribution from vertical advection to the MJO MSE budget is comparatively smaller in model-based studies (Maloney 2009; Andersen and Kuang 2012; Arnold et al. 2015).

One noticeable difference between the ERW and the MJO MSE budgets is the phase difference between the precipitation and MSE (or column-integrated moisture) perturbations. A slight quadrature relationship between these quantities is seen for the longwave ERW. This diverges from observed composites, which instead show a nearly in-phase MSE–precipitation relationship (Kiranmayi and Maloney 2011; Kim et al. 2014). Two possible sources of this discrepancy are considered. The first source is parameteric uncertainty, particularly in the reference values for the effective gross moist stability ($m_{\text{eff}}$) and the moisture sensitivity of convection ($\varepsilon_q$). This can be addressed by considering parameter regimes in the neighborhood of the reference regime (Fig. S1 in the online supplemental material). The second source is a structural limitation due to the use of a single vertical profile to represent moisture variations. For the MJO, the boundary layer moisture variations have a noticeable quadrature relationship with the precipitation, while the free-tropospheric moisture variations are more in-phase (e.g., Kiladis et al. 2005; Benedict and Randall 2007; Hsu and Li 2012). It is therefore worth exploring if an independently varying boundary layer (as in Wang and Rui 1990; Wang et al. 2016) can more accurately capture the MJO moisture–precipitation phase relationship, as well as the observed maximum in boundary layer convergence to the east of the MJO precipitation maximum (Hsu and Li 2012; de Szoeke and Maloney 2020).

The ERW is closer to being a QE mode than a moisture mode. This means that when the effective gross moist stability is positive, the ERW has a small—but nonnegligible—temperature signature. The smallness of the temperature signal is a consequence of differences in the parameterized convection's sensitivity to temperature ($\varepsilon_t$) versus moisture ($\varepsilon_q$) perturbations (A21). In the reference parameter regime, the zonal wavenumber-2 ERW has a perturbation temperature amplitude that is ~3.5 times smaller than the perturbation moisture amplitude. The MJO likewise has a small temperature signature (Lin et al. 2005; Kiladis et al. 2005). At first glance (e.g., using Figs. 7 and 9 in Kiladis et al. 2005), the MJO temperature perturbation amplitude appears about 5 times smaller than its moisture perturbation amplitude.

### b. Connections to other MJO theories

It is worth highlighting some connections between the $n = 1$ ERW perspective of the MJO and other MJO theories. The ERW is an eigenmode of the equatorial beta plane. It is therefore closely connected with the MJO-like mode reported in Emanuel (2020). As in this study, Emanuel (2020) assumes moist adiabatic temperature perturbations and associated first baroclinic vertical velocity perturbations (Khairoutdinov and Emanuel 2018). The primary difference exists in the treatment of convection—although both studies use adjustment-based closures. Emanuel (2020) uses a boundary layer quasi-equilibrium closure (Raymond 1995; Emanuel 1995); this study employs a closure based on the observed precipitation-buoyancy relationship (Ahmed and Neelin 2018; Ahmed et al. 2020). The MJO-like mode in Emanuel (2020) is destabilized by cloud–radiative feedbacks and exists even in the absence of a meridional moisture gradient. The ERW reported in this study exists without explicit destabilization by cloud–radiative effects, but only in the presence of a background meridional moisture gradient. The ERW is distinct from another prominent beta-plane MJO candidate: the moist Kelvin destabilized by WISHE (Neelin and Yu 1994; Fuchs and Raymond 2002, 2017). The ERW and the moist Kelvin, however, wave occupy the same wavenumber–frequency space, and may not be easily distinguished by spectral analyses.

In the trio-interaction theory (Wang et al. 2016; Wang and Chen 2017), the MJO horizontal structure appears as an emergent property due to a boundary layer–induced coupling between the eastward-propagating Kelvin wave and the westward-propagating Rossby wave. The dry Kelvin and Rossby wave horizontal structures are parabolic cylinder functions (Matsuno 1966; Gill 1980). These functions are part of an orthogonal basis for structures that decay away from the equator (Stechmann and Majda 2015; Ogrosky and Stechmann

2015). As such, the ERW is expected to project strongly onto dry Kelvin and Rossby wave structures. However, the dispersion relationship for the ERW demonstrates that it is a single eigenmode distinct from both the Kelvin wave and the westward-propagating Rossby wave. A mode-mode interaction—though interesting to consider—is not essential to explain either the observed horizontal structure of the MJO or its slow, eastward propagation.

The shallow-water models of Sukhatme (2014) and Suhas and Sukhatme (2020) show a slow, eastward-propagating solution. This solution emerges in the presence of a meridional moisture gradient and is destabilized upon the inclusion of a positive zonal moisture gradient. These properties are consistent with that of the ERW. Relatedly, the ERW could be also viewed as an eastward-propagating vorticity anomaly (Hayashi and Itoh 2017). An initial vorticity budget analysis (Fig. S5 in the online supplemental material) of the ERW is consistent with the mechanism posited by Hayashi and Itoh (2017)—whereby vortex stretching due to strong near-equatorial convergence overwhelms the beta effect and allows the ERW vorticity anomalies to propagate eastward. Hayashi and Itoh (2017) also appear to have anticipated the presence of two counter-propagating eigenmodes (see their Fig. 14) that are characterized by the degree of near-equatorial vortex stretching. Unlike the eastward-propagating mode in Hayashi and Itoh (2017), the ERW does not require negative gross moist stability to propagate eastward. The inclusion of a meridional moisture gradient with small positive effective gross moist stability appears to be adequate to counter the beta effect. Another difference is that Hayashi and Itoh (2017) use a vertical velocity based convective scheme, in contrast to the adjustment-based scheme employed here.

The moisture mode theory was formulated in Sobel and Maloney (2012, 2013) and improved upon by Adames and Kim (2016), who introduced the effects of a background meridional moisture gradient into the theory. The model used in this study inherits parameterizations—like for the moistening effects of zonal winds—and shares structural properties—like a single baroclinic mode vertical structure—with the model of Adames and Kim (2016). However, fundamental differences in the governing equations and assumptions separate the moisture mode and the ERW perspectives. The moisture mode theory neglects the temperature tendency term by invoking the weak temperature gradient approximation (Sobel and Bretherton 2000; Sobel et al. 2001). Moisture mode theory also neglects the momentum tendencies. The MJO horizontal wind field is assumed a priori to be given by the Matsuno–Gill response to equatorial heating, and is computed using an appropriate Green's function (Wu et al. 2001). In contrast, all the tendency terms are intact in the ERW theory, and the horizontal structure emerges as a valid eigenfunction of the problem. In the standard parameter regime, the ERW is explicitly not a moisture mode—it is instead a QE mode. The moisture mode theory requires effective gross moist instability ($m_{\text{eff}} < 0$) to render the MJO unstable; the theory also requires either diffusion (Sobel and Maloney 2012, 2013) or wavenumber-dependent gross moist stability (Adames and Kim 2016) to allow preferential growth at planetary scales. In contrast, the ERW is unstable near planetary scales for positive values of $m_{\text{eff}}$ when low-level easterlies moisten the column.

## 8. Summary

Linearized wave solutions for the equatorial beta plane are obtained in the presence of a background meridional moisture gradient. A slow, eastward-propagating mode emerges as a valid solution for a small range of zonal wavenumbers near planetary scales, with larger wavenumber solutions restricted by the meridional decay condition. This mode exhibits maximum growth rates near planetary scales. For the parameter space explored here and for zonal wavenumber 2, this mode propagates with phase speeds between 4 and 8 m s$^{-1}$. The horizontal structure of this mode consists of a low-level convergence center on the equator flanked by two off-equatorial cyclonic gyres to the west and anticyclonic gyres to the east. The strength of the off-equatorial gyres varies with zonal scale, and is weaker at larger scales. An analytic expression for the leading-order dispersion relationship of this mode is derived, and shows that:

(i) The mode phase speed is partly induced by meridional moisture advection. Additionally, the mode phase speed is smaller than dry wave speeds due to a gross moist stability variant acting as a reduced static stability for propagation.
(ii) The mode is unstable near planetary scales when low-level perturbation easterlies moisten the column.
(iii) The dispersion relationship of the mode is algebraically similar to that of the westward-propagating equatorial Rossby wave; only a sign difference separates the expressions for the two modes. In numerical solutions, this manifests as a smooth transition between the two modes across wavenumber zero.

Point (iii) suggests that the eastward-propagating mode is a counterpart of the westward-propagating equatorial Rossby wave. The mode is accordingly labeled the eastward-propagating equatorial Rossby wave (ERW). A moist static energy budget analysis shows that the ERW planetary-scale selection is partly explained by damping due to a finite convective adjustment time scale, and less effective zonal wind–induced moistening at smaller scales. Parameter perturbation experiments show that the ERW is absent when the meridional moisture gradient is too weak, and that the ERW primarily exists only for small, positive values of the effective gross moist stability. Increasing moistening strength associated with low-level easterlies increases the maximum ERW growth rates. When moistening is instead caused by low-level westerlies, the ERW solution is damped but the westward-propagating Rossby wave is unstable near planetary scales. A family of ERWs with different meridional structures—but similar dispersion curves—coexist with the $\nu = 0$ moist Kelvin wave in the low-frequency, planetary wavenumber space.

*Acknowledgments.* This research was supported by National Science Foundation Grant AGS-1936810. Discussions with Ángel Adames, Daehyun Kim, and J. David Neelin helped improve this study. Insightful reviews from Alex Gonzalez and an anonymous reviewer are gratefully acknowledged. The ERA5 data were accessed through the Copernicus Climate Data Store (https://doi.org/10.24381/cds.bd0915c6). The scripts used to obtain numerical solutions of the dispersion relationships are available upon request of the author.

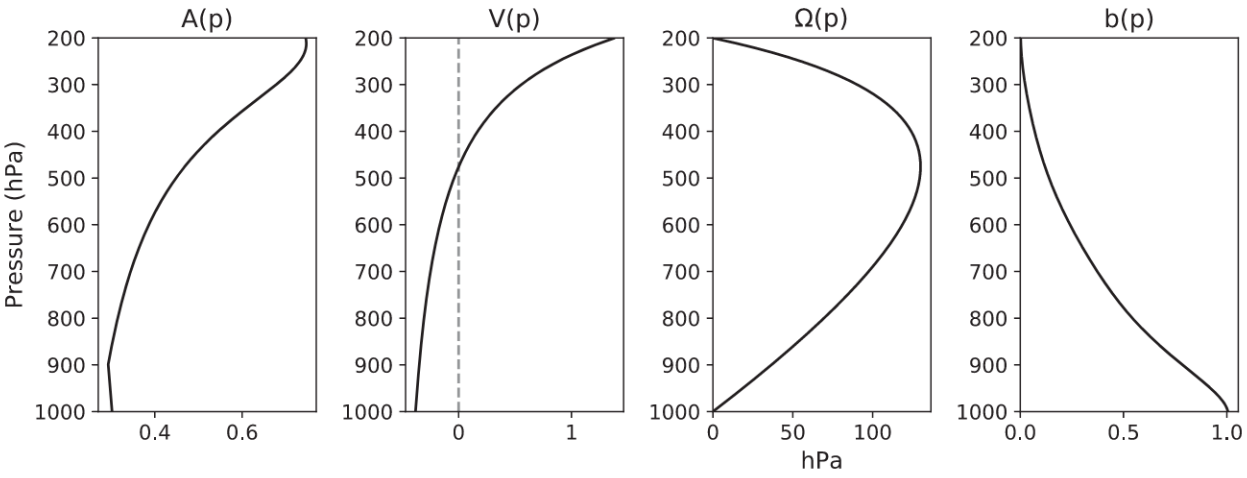


FIG. A1. Vertical structures corresponding to that of temperature ($A$), horizontal wind ($V$), vertical velocity ($\Omega$), and moisture ($b$). Except for $\Omega$, all other vertical structures are unitless.

## APPENDIX A

### Vertical and Horizontal Structures of Model Solutions

#### a. *Vertical structures*

The vertical structures used to truncate the governing equations in section 2b are shown in Fig. A1. These structures are similar to those used in Neelin and Zeng (2000), Adames and Kim (2016), and A21 among many other studies. From Fig. A1, the values of $\langle b\rangle$ and $\langle Vb\rangle$ are estimated to be 54.6 and −19.4, respectively. Using the relationship $\sigma_y = -\langle Vb\rangle\sigma_{y0}$—from (8)—and an estimate for $\sigma_{y0}\langle b\rangle$—from Fig. 1b—yields the reference value of $\sigma_y$ in Table 1.

#### b. *Reconstructing the horizontal structure*

For any given eigenmode and wavenumber $k$, knowledge of $\lambda(k)$ allows the construction of $v_1(x, y)$ using (13) and (29). To construct the complete horizontal structure of the eigenmode, the variables $u_1$, $\omega_1$, $\langle T\rangle$, and $\langle q\rangle$ must be recovered from $v_1$. The governing equations, (14), (16), (17), and (18), can used to express $u_1$ in terms of $v_1$:

$$u_1 = \frac{[\lambda(\lambda+\varepsilon_a)\beta y + ic^2k\varepsilon_q(1+r)\xi_y y]v_1 + ic^2k(\lambda+m_{\text{eff}}\varepsilon_q)\partial_y v_1}{\lambda^2(\lambda+\varepsilon_a) + ikc^2\varepsilon_q(1+r)\xi_x + c^2k^2(\lambda+m_{\text{eff}}\varepsilon_q)}. \tag{A1}$$

The construction of $u_1$ follows from (A1). The constraint that the denominator of (A1) be nonzero is used to eliminate spurious solutions when solving the $n = 0$ case. Once $u_1$ and $v_1$ are known, $\omega_1$ follows from the continuity equation, (16); $\langle T\rangle$ follows from the zonal momentum equation, (14):

$$\langle T\rangle = \frac{iM_s}{c^2k}(\lambda u_1 - \beta y v_1), \tag{A2}$$

and $\langle q\rangle$ follows from the temperature budget (17):

$$\langle q\rangle = \frac{[\lambda+\varepsilon_t(1+r)]\langle T\rangle - \omega_1 M_s}{\varepsilon_q(1+r)}. \tag{A3}$$

Once the state variables are known, the parameterized terms (precipitation, radiative heating, meridional moisture advection etc.) are recovered using the relations in section 2c.

## APPENDIX B

### Derivation of the Leading-Order Dispersion Relationship

The dispersion relationship in (28) when expressed in terms of $\lambda$ reads as follows:

$$\frac{ik\beta}{\lambda} - k^2 - \frac{\lambda^2(\lambda+\varepsilon_a)}{c^2(\lambda+m_{\text{eff}}\varepsilon_q)} - \frac{ik\varepsilon_q(1+r)\xi_x}{(\lambda+m_{\text{eff}}\varepsilon_q)} + \frac{(1+r)\varepsilon_q(\lambda\xi_y-\beta\xi_x)}{2\lambda(\lambda+m_{\text{eff}}\varepsilon_q)}$$
$$= \pm(2n+1)\sqrt{\frac{(1+r)^2\varepsilon_q^2(\beta\xi_x-\lambda\xi_y)^2}{4\lambda^2(\lambda+m_{\text{eff}})^2} + \frac{\beta^2}{c^2}\left(\frac{\lambda+\varepsilon_a}{\lambda+m_{\text{eff}}}\right)} + \frac{ik(1+r)\varepsilon_q\beta\xi_y}{\lambda(\lambda+m_{\text{eff}})}. \tag{B1}$$

The above expression can be expanded into an eighth-order polynomial in $\lambda$. To obtain approximate analytic approximations for $\lambda$ in the limiting regime of $k \to 0$, we introduce the following nondimensional parameters:

$$\lambda = \lambda^* ck, \tag{B2}$$

$$\delta = \frac{ck}{\varepsilon_q m_{\text{eff}}}. \tag{B3}$$

As in A21, $\lambda^*$ is a nondimensional frequency; $\delta$ tracks the wavenumber $k$ and measures the ratio of the gravity wave to moisture mode time scales. Using (32)–(34) and (B2)–(B3) in (B1) yields at leading order:

$$m_r(\lambda^*\eta_y + 2i - \eta_x) + O(\delta) = \pm(2n+1)\sqrt{m_r}\sqrt{4\lambda^*(\lambda^* + i\eta_y) + (\eta_x - \lambda^*\eta_y)^2 + O(\delta)}. \tag{B4}$$

In the longwave regime $\delta$ is a small parameter, so $O(\delta)$ in (B4) denotes higher terms. Simply neglecting the $O(\delta)$ terms in (B4) yields a quadratic equation with two solutions for $\lambda^*$. These solutions when redimensionalized using (B2) yield the dispersion relationship in (37).

## REFERENCES


Adames, Á. F., and J. M. Wallace, 2014: Three-dimensional structure and evolution of the vertical velocity and divergence fields in the MJO. *J. Atmos. Sci.*, **71**, 4661–4681, https://doi.org/10.1175/JAS-D-14-0091.1.

——, and ——, 2015: Three-dimensional structure and evolution of the moisture field in the MJO. *J. Atmos. Sci.*, **72**, 3733–3754, https://doi.org/10.1175/JAS-D-15-0003.1.

——, and D. Kim, 2016: The MJO as a dispersive, convectively coupled moisture wave: Theory and observations. *J. Atmos. Sci.*, **73**, 913–941, https://doi.org/10.1175/JAS-D-15-0170.1.

——, ——, S. K. Clark, Y. Ming, and K. Inoue, 2019: Scale analysis of moist thermodynamics in a simple model and the relationship between moisture modes and gravity waves. *J. Atmos. Sci.*, **76**, 3863–3881, https://doi.org/10.1175/JAS-D-19-0121.1.

——, S. W. Powell, F. Ahmed, V. C. Mayta, and J. D. Neelin, 2021: Tropical precipitation evolution in a buoyancy-budget framework. *J. Atmos. Sci.*, **78**, 509–528, https://doi.org/10.1175/JAS-D-20-0074.1.

Ahmed, F., and J. D. Neelin, 2018: Reverse engineering the tropical precipitation–buoyancy relationship. *J. Atmos. Sci.*, **75**, 1587–1608, https://doi.org/10.1175/JAS-D-17-0333.1.

——, Á. F. Adames, and J. D. Neelin, 2020: Deep convective adjustment of temperature and moisture. *J. Atmos. Sci.*, **77**, 2163–2186, https://doi.org/10.1175/JAS-D-19-0227.1.

——, J. D. Neelin, and Á. F. Adames, 2021: Quasi-equilibrium and weak temperature gradient balances in an equatorial beta-plane model. *J. Atmos. Sci.*, **78**, 209–227, https://doi.org/10.1175/JAS-D-20-0184.1.

Andersen, J. A., and Z. Kuang, 2012: Moist static energy budget of MJO-like disturbances in the atmosphere of a zonally symmetric aquaplanet. *J. Climate*, **25**, 2782–2804, https://doi.org/10.1175/JCLI-D-11-00168.1.

Arnold, N. P., M. Branson, Z. Kuang, D. A. Randall, and E. Tziperman, 2015: MJO intensification with warming in the superparameterized CESM. *J. Climate*, **28**, 2706–2724, https://doi.org/10.1175/JCLI-D-14-00494.1.

Back, L., and C. Bretherton, 2006: Geographic variability in the export of moist static energy and vertical motion profiles in the tropical Pacific. *Geophys. Res. Lett.*, **33**, L17810, https://doi.org/10.1029/2006GL026672.

Benedict, J. J., and D. A. Randall, 2007: Observed characteristics of the MJO relative to maximum rainfall. *J. Atmos. Sci.*, **64**, 2332–2354, https://doi.org/10.1175/JAS3968.1.

Bretherton, C. S., and A. H. Sobel, 2002: A simple model of a convectively coupled Walker circulation using the weak temperature gradient approximation. *J. Climate*, **15**, 2907–2920, https://doi.org/10.1175/1520-0442(2002)015<2907:ASMOAC>2.0.CO;2.

——, M. E. Peters, and L. E. Back, 2004: Relationships between water vapor path and precipitation over the tropical oceans. *J. Climate*, **17**, 1517–1528, https://doi.org/10.1175/1520-0442(2004)017<1517:RBWVPA>2.0.CO;2.

Brown, R. G., and C. Zhang, 1997: Variability of midtropospheric moisture and its effect on cloud-top height distribution during TOGA COARE. *J. Atmos. Sci.*, **54**, 2760–2774, https://doi.org/10.1175/1520-0469(1997)054<2760:VOMMAI>2.0.CO;2.

de Szoeke, S. P., and E. D. Maloney, 2020: Atmospheric mixed layer convergence from observed MJO sea surface temperature anomalies. *J. Climate*, **33**, 547–558, https://doi.org/10.1175/JCLI-D-19-0351.1.

DeMott, C. A., B. O. Wolding, E. D. Maloney, and D. A. Randall, 2018: Atmospheric mechanisms for MJO decay over the Maritime Continent. *J. Geophys. Res. Atmos.*, **123**, 5188–5204, https://doi.org/10.1029/2017JD026979.

——, N. P. Klingaman, W.-L. Tseng, M. A. Burt, Y. Gao, and D. A. Randall, 2019: The convection connection: How ocean feedbacks affect tropical mean moisture and MJO propagation. *J. Geophys. Res. Atmos.*, **124**, 11 910–11 931, https://doi.org/10.1029/2019JD031015.

Emanuel, K., 1993: The effect of convective response time on WISHE modes. *J. Atmos. Sci.*, **50**, 1763–1776, https://doi.org/10.1175/1520-0469(1993)050<1763:TEOCRT>2.0.CO;2.

Emanuel, K. A., 1987: An air–sea interaction model of intraseasonal oscillations in the tropics. *J. Atmos. Sci.*, **44**, 2324–2340, https://doi.org/10.1175/1520-0469(1987)044<2324:AASIMO>2.0.CO;2.

——, 1995: The behavior of a simple hurricane model using a convective scheme based on subcloud-layer entropy equilibrium. *J. Atmos. Sci.*, **52**, 3960–3968, https://doi.org/10.1175/1520-0469(1995)052<3960:TBOASH>2.0.CO;2.

——, 2020: Slow modes of the equatorial waveguide. *J. Atmos. Sci.*, **77**, 1575–1582, https://doi.org/10.1175/JAS-D-19-0281.1.

——, J. David Neelin, and C. S. Bretherton, 1994: On large-scale circulations in convecting atmospheres. *Quart. J. Roy. Meteor. Soc.*, **120**, 1111–1143, https://doi.org/10.1002/qj.49712051902.

Frierson, D. M. W., 2007: Convectively coupled Kelvin waves in an idealized moist general circulation model. *J. Atmos. Sci.*, **64**, 2076–2090, https://doi.org/10.1175/JAS3945.1.

Fuchs, Ž., and D. J. Raymond, 2002: Large-scale modes of a nonrotating atmosphere with water vapor and cloud–radiation feedbacks. *J. Atmos. Sci.*, **59**, 1669–1679, https://doi.org/10.1175/1520-0469(2002)059<1669:LSMOAN>2.0.CO;2.

——, and ——, 2005: Large-scale modes in a rotating atmosphere with radiative–convective instability and WISHE. *J. Atmos. Sci.*, **62**, 4084–4094, https://doi.org/10.1175/JAS3582.1.

——, and ——, 2017: A simple model of intraseasonal oscillations. *J. Adv. Model. Earth Syst.*, **9**, 1195–1211, https://doi.org/10.1002/2017MS000963.

——, S. Gjorgjievska, and D. J. Raymond, 2012: Effects of varying the shape of the convective heating profile on convectively coupled gravity waves and moisture modes. *J. Atmos. Sci.*, **69**, 2505–2519, https://doi.org/10.1175/JAS-D-11-0308.1.

Fuchs-Stone, Ž., D. J. Raymond, and S. Sentić, 2019: A simple model of convectively coupled equatorial Rossby waves.

*J. Adv. Model. Earth Syst.*, **11**, 173–184, https://doi.org/10.1029/2018MS001433.

Gill, A. E., 1980: Some simple solutions for heat-induced tropical circulation. *Quart. J. Roy. Meteor. Soc.*, **106**, 447–462, https://doi.org/10.1002/qj.49710644905.

Gonzalez, A. O., and X. Jiang, 2017: Winter mean lower tropospheric moisture over the Maritime Continent as a climate model diagnostic metric for the propagation of the Madden–Julian Oscillation. *Geophys. Res. Lett.*, **44**, 2588–2596, https://doi.org/10.1002/2016GL072430.

——, and ——, 2019: Distinct propagation characteristics of intraseasonal variability over the tropical west Pacific. *J. Geophys. Res. Atmos.*, **124**, 5332–5351, https://doi.org/10.1029/2018JD029884.

Haertel, P. T., and G. N. Kiladis, 2004: Dynamics of 2-day equatorial waves. *J. Atmos. Sci.*, **61**, 2707–2721, https://doi.org/10.1175/JAS3352.1.

Hayashi, M., and H. Itoh, 2017: A new mechanism of the slow eastward propagation of unstable disturbances with convection in the tropics: Implications for the MJO. *J. Atmos. Sci.*, **74**, 3749–3769, https://doi.org/10.1175/JAS-D-16-0300.1.

Hendon, H. H., and B. Liebmann, 1994: Organization of convection within the Madden–Julian Oscillation. *J. Geophys. Res.*, **99**, 8073–8083, https://doi.org/10.1029/94JD00045.

——, and M. L. Salby, 1994: The life cycle of the Madden–Julian Oscillation. *J. Atmos. Sci.*, **51**, 2225–2237, https://doi.org/10.1175/1520-0469(1994)051<2225:TLCOTM>2.0.CO;2.

Hersbach, H., and Coauthors, 2020: The ERA5 global reanalysis. *Quart. J. Roy. Meteor. Soc.*, **146**, 1999–2049, https://doi.org/10.1002/qj.3803.

Holloway, C. E., and J. D. Neelin, 2009: Moisture vertical structure, column water vapor, and tropical deep convection. *J. Atmos. Sci.*, **66**, 1665–1683, https://doi.org/10.1175/2008JAS2806.1.

Hsu, P., and T. Li, 2012: Role of the boundary layer moisture asymmetry in causing the eastward propagation of the Madden–Julian oscillation. *J. Climate*, **25**, 4914–4931, https://doi.org/10.1175/JCLI-D-11-00310.1.

Inoue, K., and L. Back, 2015: Column-integrated moist static energy budget analysis on various time scales during TOGA COARE. *J. Atmos. Sci.*, **72**, 1856–1871, https://doi.org/10.1175/JAS-D-14-0249.1.

——, and ——, 2017: Gross moist stability analysis: Assessment of satellite-based products in the GMS plane. *J. Atmos. Sci.*, **74**, 1819–1837, https://doi.org/10.1175/JAS-D-16-0218.1.

Jiang, X., 2017: Key processes for the eastward propagation of the Madden–Julian Oscillation based on multimodel simulations. *J. Geophys. Res. Atmos.*, **122**, 755–770, https://doi.org/10.1002/2016JD025955.

——, M. Zhao, E. D. Maloney, and D. E. Waliser, 2016: Convective moisture adjustment time scale as a key factor in regulating model amplitude of the Madden–Julian Oscillation. *Geophys. Res. Lett.*, **43**, 10 412–10 419, https://doi.org/10.1002/2016GL070898.

——, E. Maloney, and H. Su, 2020: Large-scale controls of propagation of the Madden-Julian Oscillation. *Climate Atmos. Sci.*, **3**, 29, https://doi.org/10.1038/s41612-020-00134-x.

Kang, D., D. Kim, M.-S. Ahn, R. Neale, J. Lee, and P. Glecker, 2020: The role of the mean state on MJO simulation in CESM2 ensemble simulation. *Geophys. Res. Lett.*, **47**, e2020GL089824, https://doi.org/10.1029/2020GL089824.

——, ——, ——, and S.-I. An, 2021: The role of background meridional moisture gradient on the propagation of the MJO over the maritime continent. *J. Climate*, 34, 6565–6581, https://doi.org/10.1175/JCLI-D-20-0085.1.

Kang, I.-S., F. Liu, M.-S. Ahn, Y.-M. Yang, and B. Wang, 2013: The role of SST structure in convectively coupled Kelvin–Rossby waves and its implications for MJO formation. *J. Climate*, **26**, 5915–5930, https://doi.org/10.1175/JCLI-D-12-00303.1.

Khairoutdinov, M. F., and K. Emanuel, 2018: Intraseasonal variability in a cloud-permitting near-global equatorial aquaplanet model. *J. Atmos. Sci.*, **75**, 4337–4355, https://doi.org/10.1175/JAS-D-18-0152.1.

Khouider, B., and A. J. Majda, 2006: A simple multicloud parameterization for convectively coupled tropical waves. Part I: Linear analysis. *J. Atmos. Sci.*, **63**, 1308–1323, https://doi.org/10.1175/JAS3677.1.

——, and ——, 2008: Multicloud models for organized tropical convection: Enhanced congestus heating. *J. Atmos. Sci.*, **65**, 895–914, https://doi.org/10.1175/2007JAS2408.1.

Kiladis, G. N., K. H. Straub, and P. T. Haertel, 2005: Zonal and vertical structure of the Madden–Julian oscillation. *J. Atmos. Sci.*, **62**, 2790–2809, https://doi.org/10.1175/JAS3520.1.

——, M. C. Wheeler, P. T. Haertel, K. H. Straub, and P. E. Roundy, 2009: Convectively coupled equatorial waves. *Rev. Geophys.*, **47**, RG2003, https://doi.org/10.1029/2008RG000266.

Kim, D., J.-S. Kug, and A. H. Sobel, 2014: Propagating versus nonpropagating Madden–Julian oscillation events. *J. Climate*, **27**, 111–125, https://doi.org/10.1175/JCLI-D-13-00084.1.

——, M.-S. Ahn, I.-S. Kang, and A. D. Del Genio, 2015: Role of longwave cloud–radiation feedback in the simulation of the Madden–Julian oscillation. *J. Climate*, **28**, 6979–6994, https://doi.org/10.1175/JCLI-D-14-00767.1.

——, H. Kim, and M.-I. Lee, 2017: Why does the MJO detour the Maritime Continent during austral summer? *Geophys. Res. Lett.*, **44**, 2579–2587, https://doi.org/10.1002/2017GL072643.

Kiranmayi, L., and E. D. Maloney, 2011: Intraseasonal moist static energy budget in reanalysis data. *J. Geophys. Res.*, **116**, D21117, https://doi.org/10.1029/2011JD016031.

Kuang, Z., 2008: A moisture-stratiform instability for convectively coupled waves. *J. Atmos. Sci.*, **65**, 834–854, https://doi.org/10.1175/2007JAS2444.1.

Kuo, Y.-H., J. D. Neelin, and C. R. Mechoso, 2017: Tropical convective transition statistics and causality in the water vapor–precipitation relation. *J. Atmos. Sci.*, **74**, 915–931, https://doi.org/10.1175/JAS-D-16-0182.1.

Lin, J.-L., and B. E. Mapes, 2004: Radiation budget of the tropical intraseasonal oscillation. *J. Atmos. Sci.*, **61**, 2050–2062, https://doi.org/10.1175/1520-0469(2004)061<2050:RBOTTI>2.0.CO;2.

——, M. Zhang, and B. Mapes, 2005: Zonal momentum budget of the Madden–Julian oscillation: The source and strength of equivalent linear damping. *J. Atmos. Sci.*, **62**, 2172–2188, https://doi.org/10.1175/JAS3471.1.

Madden, R. A., and P. R. Julian, 1971: Detection of a 40–50 day oscillation in the zonal wind in the tropical Pacific. *J. Atmos. Sci.*, **28**, 702–708, https://doi.org/10.1175/1520-0469(1971)028<0702:DOADOI>2.0.CO;2.

——, and ——, 1994: Observations of the 40–50-day tropical oscillation—A review. *Mon. Wea. Rev.*, **122**, 814–837, https://doi.org/10.1175/1520-0493(1994)122<0814:OOTDTO>2.0.CO;2.

Majda, A. J., and M. G. Shefter, 2001: Models for stratiform instability and convectively coupled waves. *J. Atmos. Sci.*, **58**, 1567–1584, https://doi.org/10.1175/1520-0469(2001)058<1567:MFSIAC>2.0.CO;2.

——, and S. N. Stechmann, 2009: The skeleton of tropical intraseasonal oscillations. *Proc. Natl. Acad. Sci. USA*, **106**, 8417–8422, https://doi.org/10.1073/pnas.0903367106.

Maloney, E. D., 2009: The moist static energy budget of a composite tropical intraseasonal oscillation in a climate model. *J. Climate*, **22**, 711–729, https://doi.org/10.1175/2008JCLI2542.1.

——, and M. J. Dickinson, 2003: The intraseasonal oscillation and the energetics of summertime tropical western North Pacific synoptic-scale disturbances. *J. Atmos. Sci.*, **60**, 2153–2168, https://doi.org/10.1175/1520-0469(2003)060<2153:TIOATE>2.0.CO;2.

——, A. H. Sobel, and W. M. Hannah, 2010: Intraseasonal variability in an aquaplanet general circulation model. *J. Adv. Model. Earth Syst.*, **2**, 5, https://doi.org/10.3894/JAMES.2010.2.5.

Mapes, B. E., 2000: Convective inhibition, subgrid-scale triggering energy, and stratiform instability in a toy tropical wave model. *J. Atmos. Sci.*, **57**, 1515–1535, https://doi.org/10.1175/1520-0469(2000)057<1515:CISSTE>2.0.CO;2.

Matsuno, T., 1966: Quasi-geostrophic motions in the equatorial area. *J. Meteor. Soc. Japan*, **44**, 25–43, https://doi.org/10.2151/jmsj1965.44.1_25.

Monteiro, J. M., and J. Sukhatme, 2016: Quasi-geostrophic dynamics in the presence of moisture gradients. *Quart. J. Roy. Meteor. Soc.*, **142**, 187–195, https://doi.org/10.1002/qj.2644.

Neelin, J. D., and I. M. Held, 1987: Modeling tropical convergence based on the moist static energy budget. *Mon. Wea. Rev.*, **115**, 3–12, https://doi.org/10.1175/1520-0493(1987)115<0003:MTCBOT>2.0.CO;2.

——, and J.-Y. Yu, 1994: Modes of tropical variability under convective adjustment and the Madden–Julian Oscillation. Part I: Analytical theory. *J. Atmos. Sci.*, **51**, 1876–1894, https://doi.org/10.1175/1520-0469(1994)051<1876:MOTVUC>2.0.CO;2.

——, and N. Zeng, 2000: A quasi-equilibrium tropical circulation model—Formulation. *J. Atmos. Sci.*, **57**, 1741–1766, https://doi.org/10.1175/1520-0469(2000)057<1741:AQETCM>2.0.CO;2.

——, and H. Su, 2005: Moist teleconnection mechanisms for the tropical South American and Atlantic sector. *J. Climate*, **18**, 3928–3950, https://doi.org/10.1175/JCLI3517.1.

——, I. M. Held, and K. H. Cook, 1987: Evaporation–wind feedback and low-frequency variability in the tropical atmosphere. *J. Atmos. Sci.*, **44**, 2341–2348, https://doi.org/10.1175/1520-0469(1987)044<2341:EWFALF>2.0.CO;2.

Ogrosky, H. R., and S. N. Stechmann, 2015: Assessing the equatorial longwave approximation: Asymptotics and observational data analysis. *J. Atmos. Sci.*, **72**, 4821–4843, https://doi.org/10.1175/JAS-D-15-0065.1.

Peters, M. E., and C. S. Bretherton, 2005: A simplified model of the Walker circulation with an interactive ocean mixed layer and cloud–radiative feedbacks. *J. Climate*, **18**, 4216–4234, https://doi.org/10.1175/JCLI3534.1.

Powell, S. W., 2017: Successive MJO propagation in MERRA-2 reanalysis. *Geophys. Res. Lett.*, **44**, 5178–5186, https://doi.org/10.1002/2017GL073399.

Raymond, D. J., 1995: Regulation of moist convection over the west Pacific warm pool. *J. Atmos. Sci.*, **52**, 3945–3959, https://doi.org/10.1175/1520-0469(1995)052<3945:ROMCOT>2.0.CO;2.

——, and Ž. Fuchs, 2007: Convectively coupled gravity and moisture modes in a simple atmospheric model. *Tellus*, **59A**, 627–640, https://doi.org/10.1111/j.1600-0870.2007.00268.x.

——, G. B. Raga, C. S. Bretherton, J. Molinari, C. López-Carrillo, and Ž. Fuchs, 2003: Convective forcing in the intertropical convergence zone of the eastern Pacific. *J. Atmos. Sci.*, **60**, 2064–2082, https://doi.org/10.1175/1520-0469(2003)060<2064:CFITIC>2.0.CO;2.

——, S. L. Sessions, A. H. Sobel, and Ž. Fuchs, 2009: The mechanics of gross moist stability. *J. Adv. Model. Earth Syst.*, **1** (3), https://doi.org/10.3894/JAMES.2009.1.9.

Ren, P., D. Kim, M.-S. Ahn, D. Kang, and H.-L. Ren, 2021: Intercomparison of MJO column moist static energy and water vapor budget among six modern reanalysis products. *J. Climate*, **34**, 2977–3001, https://doi.org/10.1175/JCLI-D-20-0653.1.

Rui, H., and B. Wang, 1990: Development characteristics and dynamic structure of tropical intraseasonal convection anomalies. *J. Atmos. Sci.*, **47**, 357–379, https://doi.org/10.1175/1520-0469(1990)047<0357:DCADSO>2.0.CO;2.

Schiro, K. A., F. Ahmed, S. E. Giangrande, and J. D. Neelin, 2018: GoAmazon2014/5 campaign points to deep-inflow approach to deep convection across scales. *Proc. Natl. Acad. Sci. USA*, **115**, 4577–4582, https://doi.org/10.1073/pnas.1719842115.

Shi, X., D. Kim, Á. F. Adames, and J. Sukhatme, 2018: WISHE-moisture mode in an aquaplanet simulation. *J. Adv. Model. Earth Syst.*, **10**, 2393–2407, https://doi.org/10.1029/2018MS001441.

Sobel, A. H., and C. S. Bretherton, 2000: Modeling tropical precipitation in a single column. *J. Climate*, **13**, 4378–4392, https://doi.org/10.1175/1520-0442(2000)013<4378:MTPIAS>2.0.CO;2.

——, and E. Maloney, 2012: An idealized semi-empirical framework for modeling the Madden–Julian Oscillation. *J. Atmos. Sci.*, **69**, 1691–1705, https://doi.org/10.1175/JAS-D-11-0118.1.

——, and ——, 2013: Moisture modes and the eastward propagation of the MJO. *J. Atmos. Sci.*, **70**, 187–192, https://doi.org/10.1175/JAS-D-12-0189.1.

——, J. Nilsson, and L. M. Polvani, 2001: The weak temperature gradient approximation and balanced tropical moisture waves. *J. Atmos. Sci.*, **58**, 3650–3665, https://doi.org/10.1175/1520-0469(2001)058<3650:TWTGAA>2.0.CO;2.

Stechmann, S. N., and A. J. Majda, 2015: Identifying the skeleton of the Madden–Julian oscillation in observational data. *Mon. Wea. Rev.*, **143**, 395–416, https://doi.org/10.1175/MWR-D-14-00169.1.

——, and S. Hottovy, 2017: Unified spectrum of tropical rainfall and waves in a simple stochastic model. *Geophys. Res. Lett.*, **44**, 10 713–10 724, https://doi.org/10.1002/2017GL075754.

Su, H., and J. D. Neelin, 2002: Teleconnection mechanisms for tropical Pacific descent anomalies during El Niño. *J. Atmos. Sci.*, **59**, 2694–2712, https://doi.org/10.1175/1520-0469(2002)059<2694:TMFTPD>2.0.CO;2.

Sugiyama, M., 2009: The moisture mode in the quasi-equilibrium tropical circulation model. Part I: Analysis based on the weak temperature gradient approximation. *J. Atmos. Sci.*, **66**, 1507–1523, https://doi.org/10.1175/2008JAS2690.1.

Suhas, D., and J. Sukhatme, 2020: Moist shallow-water response to tropical forcing: Initial-value problems. *Quart. J. Roy. Meteor. Soc.*, **146**, 3695–3714, https://doi.org/10.1002/qj.3867.

Sukhatme, J., 2014: Low-frequency modes in an equatorial shallow-water model with moisture gradients. *Quart. J. Roy. Meteor. Soc.*, **140**, 1838–1846, https://doi.org/10.1002/qj.2264.

Takayabu, Y. N., 1994: Large-scale cloud disturbances associated with equatorial waves Part I: Spectral features of the cloud disturbances. *J. Meteor. Soc. Japan*, **72**, 433–449, https://doi.org/10.2151/jmsj1965.72.3_433.

Tian, B., and V. Ramanathan, 2003: A simple moist tropical atmosphere model: The role of cloud radiative forcing. *J. Climate*, **16**, 2086–2092, https://doi.org/10.1175/1520-0442(2003)016<2086:ASMTAM>2.0.CO;2.

Wang, B., 1988: Dynamics of tropical low-frequency waves: An analysis of the moist Kelvin wave. *J. Atmos. Sci.*, **45**, 2051–2065, https://doi.org/10.1175/1520-0469(1988)045<2051:DOTLFW>2.0.CO;2.

——, and H. Rui, 1990: Dynamics of the coupled moist Kelvin–Rossby wave on an equatorial $\beta$-plane. *J. Atmos. Sci.*, **47**, 397–413, https://doi.org/10.1175/1520-0469(1990)047<0397:DOTCMK>2.0.CO;2.

——, and T. Li, 1994: Convective interaction with boundary-layer dynamics in the development of a tropical intraseasonal system. *J. Atmos. Sci.*, **51**, 1386–1400, https://doi.org/10.1175/1520-0469(1994)051<1386:CIWBLD>2.0.CO;2.

——, and G. Chen, 2017: A general theoretical framework for understanding essential dynamics of Madden–Julian Oscillation. *Climate Dyn.*, **49**, 2309–2328, https://doi.org/10.1007/s00382-016-3448-1.

——, F. Liu, and G. Chen, 2016: A trio-interaction theory for Madden–Julian Oscillation. *Geosci. Lett.*, **3**, 34, https://doi.org/10.1186/s40562-016-0066-z.

Wheeler, M., and G. N. Kiladis, 1999: Convectively coupled equatorial waves: Analysis of clouds and temperature in the wavenumber–frequency domain. *J. Atmos. Sci.*, **56**, 374–399, https://doi.org/10.1175/1520-0469(1999)056<0374:CCEWAO>2.0.CO;2.

——, ——, and P. J. Webster, 2000: Large-scale dynamical fields associated with convectively coupled equatorial waves. *J. Atmos. Sci.*, **57**, 613–640, https://doi.org/10.1175/1520-0469(2000)057<0613:LSDFAW>2.0.CO;2.

Wolding, B. O., and E. D. Maloney, 2015: Objective diagnostics and the Madden–Julian Oscillation. Part II: Application to moist static energy and moisture budgets. *J. Climate*, **28**, 7786–7808, https://doi.org/10.1175/JCLI-D-14-00689.1.

Wu, Z., E. Sarachik, and D. S. Battisti, 2001: Thermally driven tropical circulations under Rayleigh friction and Newtonian cooling: Analytic solutions. *J. Atmos. Sci.*, **58**, 724–741, https://doi.org/10.1175/1520-0469(2001)058<0724:TDTCUR>2.0.CO;2.

Yano, J.-I., and K. Emanuel, 1991: An improved model of the equatorial troposphere and its coupling with the stratosphere. *J. Atmos. Sci.*, **48**, 377–389, https://doi.org/10.1175/1520-0469(1991)048<0377:AIMOTE>2.0.CO;2.

Yu, J.-Y., and J. D. Neelin, 1994: Modes of tropical variability under convective adjustment and the Madden–Julian Oscillation. Part II: Numerical results. *J. Atmos. Sci.*, **51**, 1895–1914, https://doi.org/10.1175/1520-0469(1994)051<1895:MOTVUC>2.0.CO;2.

——, C. Chou, and J. D. Neelin, 1998: Estimating the gross moist stability of the tropical atmosphere. *J. Atmos. Sci.*, **55**, 1354–1372, https://doi.org/10.1175/1520-0469(1998)055<1354:ETGMSO>2.0.CO;2.

Zhang, C., 2005: Madden-Julian Oscillation. *Rev. Geophys.*, **43**, RG2003, https://doi.org/10.1029/2004RG000158.

——, and M. J. McPhaden, 2000: Intraseasonal surface cooling in the equatorial western Pacific. *J. Climate*, **13**, 2261–2276, https://doi.org/10.1175/1520-0442(2000)013<2261:ISCITE>2.0.CO;2.

——, and M. Dong, 2004: Seasonality in the Madden–Julian oscillation. *J. Climate*, **17**, 3169–3180, https://doi.org/10.1175/1520-0442(2004)017<3169:SITMO>2.0.CO;2.

——, and J. Ling, 2012: Potential vorticity of the Madden–Julian oscillation. *J. Atmos. Sci.*, **69**, 65–78, https://doi.org/10.1175/JAS-D-11-081.1.

——, Á. Adames, B. Khouider, B. Wang, and D. Yang, 2020: Four theories of the Madden-Julian Oscillation. *Rev. Geophys.*, **58**, e2019RG000685, https://doi.org/10.1029/2019RG000685.